Available online at www.sciencedirect.com
ScienceDirect
Comput. Methods Appl. Mech. Engrg. 347 (2019) 957–982
Computer methods in applied mechanics and engineering
www.elsevier.com/locate/cma

A variational phase-field model for hydraulic fracturing in porous media

Chukwudi Chukwudozie[a], Blaise Bourdin[b], Keita Yoshioka[c,*]

[a] Craft & Hawkins Department of Petroleum Engineering, Louisiana State University, Baton Rouge, LA 70803, USA
[b] Department of Mathematics and Center for Computation & Technology, Louisiana State University, Baton Rouge, LA 70803, USA
[c] Department of Environmental Informatics, Helmholtz Centre for Environmental Research – UFZ, Leipzig, Germany

Received 8 August 2018; received in revised form 6 December 2018; accepted 23 December 2018
Available online 18 January 2019

Highlights

- A unified fracture - porous medium flow model has been proposed, which is regularized with a phase-field variable consistent with the fracture mechanics regularization without defining extra variables or level set functions.
- The methodology to compute the crack opening displacement using the gradient of the phase-field variable has been derived using the Gamma-convergence approximation.
- Additionally, we point out erroneous crack opening displacement computation under deformed domain, which has not been discussed before, and propose an approach to mitigate this error.
- The proposed model has been verified in the toughness dominated regime of hydraulic fracturing.

Abstract

Rigorous coupling of fracture–porous medium fluid flow and topologically complex fracture propagation is of great scientific interest in geotechnical and biomechanical applications. In this paper, we derive a unified fracture–porous medium hydraulic fracturing model, leveraging the inherent ability of the variational phase-field approach to fracture to handle multiple cracks interacting and evolving along complex yet, critically, unspecified paths. The fundamental principle driving the crack evolution is an energetic criterion derived from Griffith's theory. The originality of this approach is that the crack path itself is derived from energy minimization instead of additional branching criterion. The numerical implementation is based on a regularization approach similar to a phase-field model, where the cracks location is represented by a smooth function defined on a fixed mesh. The derived model shows how the smooth fracture field can be used to model fluid flow in a fractured porous medium. We verify the proposed approach in a simple idealized scenario where closed form solutions exist in the literature. We then demonstrate the new method's capabilities in more realistic situations where multiple fractures turn, interact, and in some cases, merge with other fractures.

Keywords: Phase-field models of fracture; Hydraulic fracturing; Variational approach

* Corresponding author.
E-mail addresses: chdozie@gmail.com (C. Chukwudozie), bourdin@lsu.edu (B. Bourdin), keita.yoshioka@ufz.de (K. Yoshioka).

https://doi.org/10.1016/j.cma.2018.12.037
0045-7825/

1. Introduction

Understanding the physical behavior of hydraulic fracturing is not only important in geophysical processes such as dikes driven by magma [1,2] but also in geotechnical applications including environmental remediation [3], geomechanical integrity of underground storage [4,5], mining operation [6], wellbore drilling [7], productivity enhancements in hydrocarbon reservoirs [8], and the stimulation of geothermal reservoirs [9–11].

Many of the early works have made assumptions in fracture geometries, constraining fracture propagation paths to known directions and restricting the propagation on a single plane to simplify modeling of the hydraulic fracturing process. In addition, fracture fluid loss is normally assumed unidirectional while the coupled effect of fluid loss and poroelastic deformation on hydraulic fracture propagation is rarely considered. For a review of planar fracture models, readers are referred to Adachi et al. [12] and references therein. Recently, non-planar complex fracturing behaviors induced by in-situ stresses, heterogeneity in rock properties, or interaction with multiple fractures and existing discontinuities have been observed in hydraulic fracturing stimulation [13,14] and hydrothermal experiments in the earth crust condition [15]. Even in isothermal condition for single phase fluid, a comprehensive mathematical model for hydraulic fracturing analysis will require incorporation of all of the following five mechanisms [16–18]; fracture fluid flow, fluid flow in porous medium, fracture mechanics, solid deformation and poroelasticity.

The computational challenges stem from the fact that fracture propagation is a free discontinuity problem in which the fractures are considered as lower dimensional elements. As a result, it is not trivial to computationally represent fractures in the porous medium in a way that permits solution of the individual flow models on each subdomain while ensuring hydraulic communication between fractures and porous medium. Where attempts have been made to represent fractures and porous medium within the same domain, the numerous assumptions limit the ability of the models to reproduce the complex fracture behaviors. For example, special interface elements called zero-thickness elements have been used to handle fluid flow in fractures embedded in continuum media (see [19–24]). This type of elements allows for explicit fracture representation and easy solution of porous medium and fracture models in their respective computational subdomains. However, as the interface elements are inserted along the edges of continuum grids, the fracture propagation is constrained to the prescribed direction, in most cases, one of the principal coordinates. For other techniques that explicitly differentiate the fracture from the reservoir, the computational cost is expensive and the numerics cumbersome, characterized by continuous remeshing to provide grids that explicitly match the evolving fracture surface [25,26]. As an implicit approach, extended finite element method (XFEM) has been applied to the simulation of hydraulic fracturing [27–30]. However, its complex numerical implementation especially in three dimensions and the fracture propagation criteria for branching or merging still remain great challenges. Beyond conventional boundary or finite element based approaches, a non-local peridynamics method [31] and lattice based method [32,33] have also been applied, but the mesh/lattice discretization dependent fracture topology is yet to be overcome.

The variational phase-field model of fracture, which was originally proposed in the 90's [34–36], has seen explosive applications ranging from dynamic fracture [37–39], to ductile fracture [40–42], to thermal and drying fracture [43–45]. One of the strengths of this approach is to account for arbitrary numbers of pre-existing or propagating cracks in terms of energy minimization, without any a priori assumption on their geometry or restriction on the growth to specific grid directions.

The variational phase-field approach has been applied to the simulation of hydraulic fracturing for the first time in [46,47] where the model was verified for fracture propagation in impermeable and elastic medium, due to injection of inviscid fluid. In [48], the phase-field model has been further extended to porous media using the augmented Lagrangian method for fracture irreversibility and its quasi-static scheme is analyzed in details in [49]. The quasi-monolithic solution scheme and the primal–dual active set method for the fracture irreversibility along with mesh adaptivity were proposed in [50]. While the pressures in the fracture and the porous medium were distinguished, each of the pressure profiles was considered uniform throughout the domain(s) in these models. Phase-field fracture models coupled with the Darcy–Reynolds flow were proposed in [41,45,51–55] and with Darcy–Stokes type in [56–58]. Mikelić et al. [51,52] applied an indicator function based on the phase-field variable to the fracture-reservoir diffraction system. The system is solved in a fully coupled manner in [52] and the fracture width computed using a level-set in [55] for computational efficiency. In [41,45], the phase-field variable was used as a weight function to homogenize the permeability in the system. A similar homogenization approach was also taken by [54] as well as considering another phase-field variable for inclusion of interfaces. Santillán et al. [53] applied Reynolds flow equation in a 1D domain externally constructed out of the main computational domain based on a certain value of

the phase-field variable. Heider and Markert [58] and Ehlers and Luo [57] proposed the phase-field fracture modeling embedded in the Theory of Porous Media (TPM) where the phase-field variable was used to weigh between the Darcy flow in porous media and the Stokes flow in fracture. Alternatively, coupling with fluid flow has been achieved by linking to an external standalone fluid flow simulator in [59,60] where again the phase-field variable was used to distinguish the fracture domain through the permeability multiplier.

Instead of applying the phase-field variable as an indicator or constructing weighting functions from it, the present study derives a unified fracture–porous medium flow model by following the phase-field calculus (*i.e.* the phase-field variable as a regularizing function). Fluid flow in the porous medium is modeled using the poroelasticity continuity equation with Darcy's law while fracture fluid flow follows Reynolds equation with the cubic law as the equation of state. Exchange of fluid between the fracture and porous medium is considered, leading to the derivation of a tightly coupled model for fluid flow in the fracture and porous medium. Iterative solution of the variational fracture model and the coupled flow model provides a simplified framework for simultaneous modeling of rock deformation and fluid flow during hydraulic fracturing. The primary quantities of interest are the fluid pressure, fracture geometry (length, height, radius) and fracture propagation paths which are obtained from the solutions of the coupled flow and mechanical models. We verify our model by comparing numerical results with analytical solutions in the storage-toughness dominated region (K-regime) proposed by [61]. We also analyze the role of permeability and three-dimensional layered fracture toughness on fracture geometry, propagation paths and fluid diffusion profile during hydraulic fracturing. Since the phase-field technique removes the limitation of knowing a priori, fracture propagation directions, we use the model to highlight stress shadow effect during propagation of multiple hydraulic fractures.

The outline of the paper is as follows. The governing equations for the variational phase-field fracture model, fracture and porous medium fluid flows are first presented. Next, we outline the fracture width computation algorithm and present our modified fixed stress splitting scheme used for decoupling and iteratively solving the flow and mechanical models. Thereafter, the model is applied to the propagation of KGD and penny-shaped fractures. Numerical results are presented and analyzed.

2. Governing equations for the coupled system

Consider a poroelastic medium occupying a region $\Omega \subset \mathbb{R}^N$ of space. Let Γ be a known set of fractures, *i.e.* a set of two dimensional surfaces in Ω. We assume that the pore and fracture spaces are fully occupied by a single phase Newtonian fluid, and that the same fluid is being injected.

2.1. Fracture fluid flow model

In the fracture system, we make the classical assumption of a planar laminar flow following the cubic law and the generalized Reynolds equation [62,63] which accounts for different orientations along the fracture path from lubrication theory [64]. Denoting by w the fracture aperture, we have then that

$$\frac{\partial w}{\partial t} + \nabla_\Gamma \cdot (w\,\vec{q}_f) + q_l = q_{fs} \qquad \text{in } \Gamma, \tag{1}$$

$$w\vec{q}_f = -\frac{w^3}{12\mu}\nabla_\Gamma p_f \qquad \text{in } \Gamma, \tag{2}$$

$$q_l = -[\![\vec{q}_r]\!] \cdot \vec{n}_\Gamma \qquad \text{on } \Gamma, \tag{3}$$

$$\vec{q}_f \cdot \vec{\tau}_\Gamma = 0 \qquad \text{on } \partial\Gamma. \tag{4}$$

In the above equations, n_Γ and τ_Γ denote the normal and tangent vector to Γ, $\vec{q}_f$ is the fluid velocity in the fracture, $\vec{q}_r$ is the fluid velocity in the porous medium, p_f is the fluid pressure in the fracture, μ is the fluid viscosity, and q_l is the rate of leak-off between the fracture and the porous medium. Using the definition of surface divergence and substituting (2) into (1), the continuity equation for fluid pressure becomes

$$\frac{\partial w}{\partial t} - \left[(\vec{n}_\Gamma \times \nabla_\Gamma) \cdot \frac{w^3}{12\mu}(\vec{n}_\Gamma \times \nabla_\Gamma p_f)\right] + q_l = q_{fs}. \tag{5}$$

Multiplying by a test function $\psi_f \in H^1(\Gamma)$ and integrating over Γ, we obtain the weak form of (5):

$$\int_\Gamma \frac{w^3}{12\mu}\nabla_\Gamma\, p_f \cdot \nabla_\Gamma\, \psi_f\, dS = \int_\Gamma \psi_f \left(q_{fs} - \frac{\partial w}{\partial t} - q_l\right) dS. \tag{6}$$

2.2. Porous medium fluid flow model

The governing equation for flow in the porous medium adjacent to the fracture is the continuity equation from poroelasticity theory for a single phase, slightly compressible fluid [65–67]. Let q_{rs} be source or sink terms in the porous medium $\Omega \setminus \Gamma$, with a unit of volumetric flow rate per unit volume. Assuming a prescribed pressure $\bar{p}$ on $\partial_D \Omega$ and a prescribed normal flux q_n on $\partial_N^f \Omega = \partial\Omega \setminus \partial_D^f \Omega$, we have

$$\frac{\partial \zeta}{\partial t} + \nabla \cdot \vec{q}_r = q_{rs} \qquad \text{in } \Omega \setminus \Gamma, \tag{7}$$

$$\zeta = \alpha \nabla \cdot \vec{u} + \frac{p_r}{M} \qquad \text{in } \Omega \setminus \Gamma, \tag{8}$$

$$\vec{q}_r = -\frac{K}{\mu} \nabla p_r \qquad \text{in } \Omega \setminus \Gamma, \tag{9}$$

$$p_r = \bar{p} \qquad \text{on } \partial_D^f \Omega, \tag{10}$$

$$\vec{q}_r \cdot n = q_n \qquad \text{on } \partial_N^f \Omega, \tag{11}$$

where $\vec{q}_r$ is the porous medium flow rate related to the pore-pressure p_r through Darcy's law (9), K is the permeability tensor, α is the Biot's coefficient, and M is the Biot's modulus.

Upon substituting (9) into (7), the continuity equation in terms of pore-pressure becomes

$$\frac{\partial \zeta}{\partial t} - \nabla \cdot \frac{K}{\mu} \nabla p_r = q_{rs}. \tag{12}$$

We can write (12) by multiplying both terms by a test function, $\psi_r \in H^1(\Omega \setminus \Gamma)$ such that $\psi_r = 0$ on $\partial_D \Omega$, and integrating over $\Omega \setminus \Gamma$. Using Green's formula, and (3), we have that

$$\begin{aligned} -\int_{\Omega\setminus\Gamma} \nabla \cdot \frac{K}{\mu} \nabla p_r \psi_r \, dV = &\int_{\Omega\setminus\Gamma} \frac{K}{\mu} \nabla p_r \cdot \nabla \psi_r \, dV - \int_{\partial\Omega_N} \frac{K}{\mu} \nabla p_r \cdot n \psi_r \, dS \\ &- \int_{\Gamma^+} \frac{K}{\mu} (\nabla p_r)^+ \cdot n_{\Gamma^+} \psi_r^+ \, dS - \int_{\Gamma^-} \frac{K}{\mu} (\nabla p_r)^- \cdot n_{\Gamma^-} \psi_r^- \, dS, \end{aligned}$$

where $\Gamma^\pm$ denote each side of Γ, $\psi_r^\pm$ and $(\nabla p_r)^\pm$ the trace of ψ_r and ∇p_r and $n_{\Gamma^\pm}$ the outer normal vector to Ω along $\Gamma^\pm$, respectively. Using (9) and (11), we then get that

$$-\int_{\Omega\setminus\Gamma} \nabla \cdot \frac{K}{\mu} \nabla p_r \psi_r \, dV = \int_{\Omega\setminus\Gamma} \frac{K}{\mu} \nabla p_r \cdot \nabla \psi_r \, dV - \int_{\partial\Omega_N} q_n \psi_r \, dS - \int_{\Gamma} [\![\vec{q}_r]\!] \cdot n_\Gamma [\![\psi_r]\!] \, dS,$$

with the convention that n_Γ is the normal vector to Γ pointing from Γ^- to Γ^+.

Using the expression above, the porous medium flow continuity equation (12) becomes

$$\begin{aligned} &\int_{\Omega\setminus\Gamma} \frac{\partial \zeta}{\partial t} \psi_r \, dV + \int_{\Omega\setminus\Gamma} \frac{K}{\mu} \nabla p_r \cdot \nabla \psi_r \, dV = \\ &\int_{\Omega\setminus\Gamma} q_{rs} \, \psi_r \, dV - \int_{\partial_N \Omega} q_n \, \psi_r \, dS + \int_{\Gamma} [\![\vec{q}_r]\!] \cdot n_\Gamma [\![\psi_r]\!] \, dS. \end{aligned} \tag{13}$$

2.3. Combined flow equation

Traditionally, the reservoir and crack pressure are linked through leak-off law, derived empirically [68] or in specific asymptotic regimes [69]. In particular, Carter's leak-off law can be derived by assuming constant height and width and neglecting the pore pressure on the diffusion process of the injection fluid in the formation. In many applications, however, it is not clear if this assumption is reasonable. In [70], for instance, the net pressure difference between fracture and formation is approximately 20–35 MPa while the pore pressure is 40–50 MPa. In conventional reservoir, the ratio of the fracture over pore pressure is even smaller. Instead of using an ad-hoc leak-off law, we propose to combine (6) and (13) by identifying p_f, the thickness averaged pressure in the fracture, and p_r, *i.e.* neglecting the effect of the net pressure difference. This may of course lead to underestimating the amount of fluid leaking-off the fracture. In the near toughness dominated regime, when the pressure gradient through the thickness of the crack is small, we expect this approximation to be reasonable.

Under this assumption, we have that $p_r = p_f$ in Γ, so that the admissible test functions ψ_r need to be continuous across Γ, and using (3), the leak-off terms cancel out, and we obtain the combined porous medium and fracture flow equation in weak form:

$$\int_{\Omega\setminus\Gamma} \frac{\partial\zeta}{\partial t}\,\psi\,dV + \frac{K}{\mu}\int_{\Omega}\nabla p\cdot\nabla\psi\,dV + \int_{\Gamma}\frac{w^3}{12\mu}\nabla_{\Gamma}p\cdot\nabla_{\Gamma}\psi\,dS = \int_{\Omega\setminus\Gamma} q_{rs}\,\psi\,dV - \int_{\partial_N\Omega} q_n\psi\,dS + \int_{\Gamma} q_{fs}\psi\,dS - \int_{\Gamma}\frac{\partial w}{\partial t}\psi\,dS. \tag{14}$$

2.4. Mechanical equilibrium

We follow the formalism of Francfort and Marigo to derive the mechanical equilibrium and crack propagation law. In all that follows, we assume a brittle–elastic porous medium and denote by $\mathbf{A}$ and G_c its Hooke's law and fracture toughness. Assume for the moment that the pressure field p and fluid-filled crack Γ are given. Let $\partial^m_N\Omega$ be a portion of its boundary and $\partial^f_D\Omega := \partial\Omega\setminus\partial^m_N\Omega$ the remaining part. Following the classical formalism of Biot [65], we introduce a poroelastic effective stress $\sigma^{eff} := \sigma(\vec{u}) - \alpha p\mathrm{I}$, $\vec{u}$ denoting the deformation field in the porous medium, I the identity matrix in $\mathbb{R}^N$, σ the Cauchy stress, and p the pore pressure from (14). The constitutive relation for a poro-elastic material reads

$$\sigma^{eff} := \mathbf{A}\mathrm{e}(\vec{u}), \tag{15}$$

where $\mathrm{e}(\vec{u}) := \frac{\nabla\vec{u}+\nabla\vec{u}^t}{2}$ is the linearized strain. Static equilibrium and continuity of stress at the interfaces mandate that

$$-\nabla\cdot\sigma(\vec{u}) = \vec{f} \quad \text{in } \Omega\setminus\Gamma, \tag{16}$$

$$\sigma\cdot\vec{n} = \vec{\tau} \quad \text{on } \partial\Omega^m_N, \tag{17}$$

$$\vec{u} = \vec{u}_0 \quad \text{on } \partial\Omega^m_D, \tag{18}$$

$$\sigma^{\pm}\cdot\vec{n}_{\Gamma^{\pm}} = -p\vec{n}_{\Gamma^{\pm}} \quad \text{on } \Gamma^{\pm}, \tag{19}$$

where $\vec{f}$ denotes an external body force and $\vec{\tau}$ is a traction force applied to a portion $\partial^m_N\Omega$ of $\partial\Omega$. Let $\vec{u}_0$ be a given boundary displacement on $\partial^m_D\Omega := \partial\Omega\setminus\partial^m_N\Omega$.

Multiplying (16) by a test function $\vec{\phi}\in H^1(\Omega\setminus\Gamma)$ vanishing on $\partial\Omega^m_D$ and using Green's formula and (17) and (19), we get that

$$\int_{\Omega\setminus\Gamma}\mathbf{A}\left(\mathrm{e}(\vec{u}) - \frac{\alpha}{N\kappa}p\mathrm{I}\right)\cdot\mathrm{e}(\vec{\phi})\,dV = \int_{\partial\Omega^m_N}\vec{\tau}\cdot\vec{\phi}\,dS - \int_{\Gamma} p\left[\!\left[\vec{\phi}\cdot\vec{n}_{\Gamma}\right]\!\right]dS + \int_{\Omega\setminus\Gamma}\vec{f}\cdot\vec{\phi}\,dV,$$

where $N = 2$ and $N = 3$ for two and three dimensions respectively and κ denotes the material's bulk modulus. We finally recall that given p and Γ, the previous relation is just the first order optimality condition for the unique solution of the minimization among all kinematically admissible displacement of

$$\mathcal{P}(\vec{u},\Gamma;p) := \int_{\Omega\setminus\Gamma} W(\mathrm{e}(\vec{u}),p)\,dV - \int_{\partial\Omega^m_N}\vec{\tau}\cdot\vec{u}\,dS + \int_{\Gamma} p\,[\![\vec{u}\cdot\vec{n}_{\Gamma}]\!]\,dS - \int_{\Omega\setminus\Gamma}\vec{f}\cdot\vec{u}\,dV, \tag{20}$$

where

$$W(\mathrm{e}(\vec{u}),p) := \frac{1}{2}\mathbf{A}\left(\mathrm{e}(\vec{u}) - \frac{\alpha}{N\kappa}p\mathrm{I}\right)\cdot\left(\mathrm{e}(\vec{u}) - \frac{\alpha}{N\kappa}p\mathrm{I}\right) \tag{21}$$

is the poroelastic strain energy density.

Following Francfort and Marigo's variational approach to brittle fracture [34], to *any* displacement field $\vec{u}$ and crack configuration Γ (a two-dimensional surface in three space dimension or a curve in two dimensions), one can associate the total energy

$$\mathcal{F}(\vec{u},\Gamma;p) = \mathcal{P}(u,\Gamma;p) + G_c\mathcal{H}^{N-1}(\Gamma), \tag{22}$$

where G_c is the material's critical surface energy release rate and $\mathcal{H}^{N-1}(\Gamma)$ denotes the $N-1$ dimensional Hausdorff measure of Γ, that is, its aggregate surface in three dimensions and aggregate length in two dimensions. In a discrete time setting, identifying the displacement reduces to minimizing $\mathcal{F}$ with respect to any kinematically admissible displacement and crack set satisfying a growth constraint.

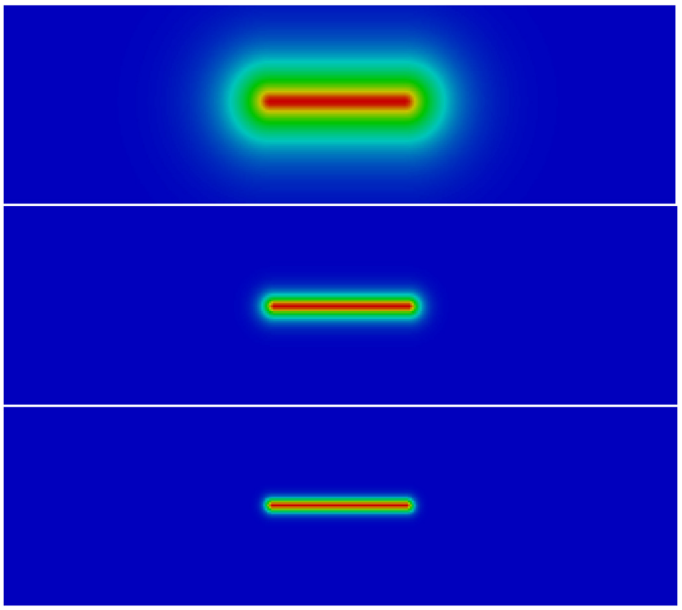

Fig. 1. Phase-field representation v of a line crack for decreasing values of the regularization length ε. The blue region corresponds to $v \simeq 1$ and the crack faces correspond to the transition regions from blue to red . (For interpretation of the references to color in this figure legend, the reader is referred to the web version of this article.)

3. Phase-field approximation

The numerical implementation of the minimization of (22) involves handling of displacement fields that are discontinuous across unknown discontinuity surfaces (the cracks), which can be challenging when using standard numerical tools. Instead, we propose to adapt the now-classical phase-field approach [35,36] based on the work of Ambrosio and Tortorelli in image segmentation [71,72], which we briefly recall in the case of an elastic material *i.e.* for $p \equiv 0$.

3.1. Variational phase-field models of fracture

Let $\varepsilon > 0$ be a regularization parameter with the dimension of a length, and $v : \Omega \mapsto [0, 1]$ be a scalar function. We define

$$\mathcal{F}_\varepsilon(\vec{u}, v; 0) = \int_\Omega W(\mathrm{e}(\vec{u}), v; 0) dV - \int_{\partial^m_N \Omega} \vec{\tau} \cdot \vec{u}\, dS - \int_\Omega \vec{f} \cdot \vec{u}\, dV + \frac{G_c}{4c_n} \int_\Omega \left(\frac{(1-v)^n}{\varepsilon} + \varepsilon |\nabla v|^2 \right) dV, \tag{23}$$

where $W(\mathrm{e}(\vec{u}), v; 0) = \frac{1}{2} v^2 \mathbf{A}\mathrm{e}(\vec{u}) \cdot \mathrm{e}(\vec{u})$, $c_n := \int_0^1 (1-s)^{n/2} ds$ $(n = 1, 2)$ is a normalization parameter. We typically refer to the case $n = 1$ as the $\mathtt{AT}_1$ energy and to $n = 2$ as $\mathtt{AT}_2$.

It can then be shown [71–73] that as ε approaches 0, the minimizers of (23) approach that of (22) in the sense that the phase-field function v takes value 1 far from the crack Γ and transitions to 0 in a region of thickness of order ε along each crack faces of Γ. Fig. 1 shows the phase-field v representing a simple straight crack in a two-dimensional domain, for decreasing values of the regularization length ε.

3.2. Extension to poroelastic media

In the context of crack propagation in a poroelastic medium, the variational model (22) and phase-field approximation (23) must be modified to account for poroelasticity and pressure forces along the fracture faces. As

in [46,47], we approximate the work of the pressure forces acting along each side of the cracks by

$$\int_\Gamma p(x)\,[\![\vec{u}(x)]\!]\cdot\vec{n}_\Gamma\,dS \simeq \int_\Omega p(x)\,\vec{u}(x)\cdot\nabla v(x)\,dV.$$

The convergence proof is technical, but the following argument illustrates how the approximation takes place.

We first recall the construction of the *optimal profile problem* [36,73], which is the construction of a function ω_ε minimizing $\int_0^\infty \frac{(1-\omega)^n}{\varepsilon} + \varepsilon(\omega')^2\,dx$ amongst all functions ω such that $0 \le \omega(x) \le 1$ on $(0,\infty)$, $\omega(0) = 0$, and $\omega(\infty) = 1$. Using a simple change of variable, it is easy to see that $\omega_\varepsilon(x) = \tilde{\omega}(\tilde{x})$, where $\tilde{x} = x/\varepsilon$, and $\tilde{\omega}$ minimizes $\int_0^\infty (1-\tilde{\omega})^n + (\tilde{\omega}')^2\,d\tilde{x}$ amongst all functions $\tilde{\omega}$ such that $0 \le \tilde{\omega}(\tilde{x}) \le 1$ on $(0,\infty)$, $\tilde{\omega}(0) = 0$, and $\tilde{\omega}(1) = 1$. Remark that the first integral associated with the optimality conditions of the optimal profile problem are $\left(\tilde{\omega}'\right)^2 = (1-\tilde{\omega})^n$, and that we recover the well known optimal profile $\omega_2(x) := 1 - e^{-|x|/\varepsilon}$ for the $\mathtt{AT}_2$ model and $\omega_1(x) = 1 - \left(1 - \frac{|x|}{2\varepsilon}\right)^2$ if $|x| \le 2\varepsilon$ and $\omega_1(x) = 1$ otherwise for the $\mathtt{AT}_1$ model.

For small enough ε, the phase-field function v_ε is well approximated by $v_\varepsilon(x) := \tilde{\omega}(d_\Gamma(x)/\varepsilon)$, where $d_\Gamma(x) := \mathrm{dist}(x,\Gamma)$. Consider then a function $\vec{\Phi}(x)$ defined on Ω and admitting traces $\vec{\Phi}^+$ and $\vec{\Phi}^-$ on each side of Γ. Using the co-area formula (a generalized version of Fubini's theorem [74]), we have

$$\begin{aligned}
\int_\Omega \vec{\Phi}(x)\cdot\nabla v_\varepsilon(x)\,dV &= \int_\Omega \frac{1}{\varepsilon}\tilde{\omega}'\left(\frac{d_\Gamma(x)}{\varepsilon}\right)\vec{\Phi}(x)\cdot\nabla d_\Gamma(x)\,dV\\
&= \int_0^\infty \int_{\{x\in\Omega;\ d_\Gamma(x)=s\}} \frac{1}{\varepsilon}\tilde{\omega}'\left(\frac{s}{\varepsilon}\right)\vec{\Phi}(x)\cdot\nabla d_\Gamma(x)\,d\mathcal{H}^{n-1}(x)\,ds\\
&= \int_0^\infty \frac{1}{\varepsilon}\tilde{\omega}'\left(\frac{s}{\varepsilon}\right)\int_{\{x\in\Omega;\ d_\Gamma(x)=s\}} \vec{\Phi}(x)\cdot\nabla d_\Gamma(x)\,d\mathcal{H}^{n-1}(x)\,ds\\
&= \int_0^\infty \tilde{\omega}'(\tilde{s})\int_{\{x\in\Omega;\ d_\Gamma(x)=\varepsilon\tilde{s}\}} \vec{\Phi}(x)\cdot\nabla d_\Gamma(x)\,d\mathcal{H}^{n-1}(x)\,d\tilde{s},
\end{aligned}$$

with $\tilde{s} = s/\varepsilon$. Formally, and under some mild regularity assumptions on Γ, when $\varepsilon \to 0$, the inner integral becomes an integral along each side of Γ, and ∇d_Γ becomes the oriented normal on each side of Γ, so that

$$\lim_{\varepsilon\to 0}\int_\Omega \vec{\Phi}(x)\cdot\nabla v_\varepsilon(x)\,dV = \int_\Gamma [\![\vec{\Phi}(x)]\!]\cdot\vec{n}_\Gamma\,dS. \tag{24}$$

Taking $\Phi(x) = p(x)\vec{u}(x)$, we recover our claim that

$$\lim_{\varepsilon\to 0}\int_\Omega p(x)\vec{u}(x)\cdot\nabla v_\varepsilon(x)\,dV = \int_\Gamma p(x)\,[\![\vec{u}(x)]\!]\cdot\vec{n}_\Gamma\,dS.$$

Remark 1. Another way to view (24) is to decompose

$$\int_\Omega \vec{\Phi}(x)\cdot\nabla v_\varepsilon(x)\,dV = \int_\Omega \vec{\Phi}(x)\cdot\frac{\nabla v_\varepsilon(x)}{|\nabla v_\varepsilon(x)|}|\nabla v_\varepsilon(x)|\,dV,$$

and think of $\nabla v_\varepsilon(x)/|\nabla v_\varepsilon(x)|$ as an approximation of $\vec{n}_{\Gamma\pm}$ and of $|\nabla v_\varepsilon(x)|$ as a measure concentrating along Γ.

The next step is to account for the phase-field variable in the poroelastic energy density W. The main modeling choice is whether the phase-field variable should affect the Cauchy or the poroelastic effective stress. Although it can be shown that both choices coincide in the limit of $\varepsilon \to 0$, we use the former. This choice is consistent with the current interpretation of the phase-field variable as a damage variable and the regularization length as a material internal length [75–77], under the modeling assumption that damage arises at the sub pore scale, *i.e.* is induced by strong Cauchy stresses. Our choice of the regularized strain energy density is therefore

$$W(\mathrm{e}(\vec{u}), v;\, p) := \tfrac{1}{2}\mathbf{A}\left(v\mathrm{e}(\vec{u}) - \frac{\alpha p}{N\kappa}\mathrm{I}\right)\cdot\left(v\mathrm{e}(\vec{u}) - \frac{\alpha p}{N\kappa}\mathrm{I}\right), \tag{25}$$

and for a given pressure field, the displacement and phase-field variables are given as the minimizer of

$$\begin{aligned}
\mathcal{F}_\varepsilon(\vec{u}, v;\, p) = &\int_\Omega W(\mathrm{e}(\vec{u}), v;\, p)\,dV - \int_{\partial_N\Omega}\vec{\tau}\cdot\vec{u}\,dS - \int_\Omega \vec{f}\cdot\vec{u}\,dV + \int_\Omega p\,\vec{u}\cdot\nabla v\,dV\\
&+\frac{G_c}{4c_n}\int_\Omega\left(\frac{(1-v)^n}{\varepsilon} + \varepsilon|\nabla v|^2\right)dV
\end{aligned} \tag{26}$$

Note that Biot's poroelasticity model can be seen as an upscaled model of a fluid–structure interaction problem, when the pore size asymptotically approaches 0, so that the argument above holds provided that ε approaches 0 slower than the pore size.

3.3. Phase-field approximation of the flow model

Since our mechanical model relies on a phase-field representation of the fracture set Γ, we need to adapt our coupled flow equation (14).

The main difficulty here is the approximation of the term originating from the fracture flow $\int_\Gamma \frac{w^3}{12\mu}\nabla_\Gamma p \cdot \nabla_\Gamma \psi \, dS$. Following the logic of Remark 1, we use the following approximation for the surface gradients:

$$\nabla_\Gamma p \simeq \nabla_\Gamma^\varepsilon p := \nabla p - \left(\nabla p \cdot \frac{\nabla v}{|\nabla v|}\right)\frac{\nabla v}{|\nabla v|}. \tag{27}$$

Integrating on Γ against w^3 is more complicated, and cannot be obtained by a direct application of (24). Proper care has to be exerted in order to properly recover $\left(\llbracket \vec{u}\cdot n \rrbracket\right)^3$ and not $\llbracket (\vec{u}\cdot n)^3 \rrbracket$. Assuming that w_ε is such that $w_\varepsilon(x) = \llbracket u(x)\cdot n_\Gamma \rrbracket$ on Γ, *i.e.* a "regularized fracture aperture", we propose the following approximation:

$$\int_\Gamma \frac{w^3}{12\mu}\nabla_\Gamma\, p \cdot \nabla_\Gamma\, \psi \, dS \simeq \int_\Omega \frac{w_\varepsilon^3}{12\mu}\nabla_\Gamma^\varepsilon\, p \cdot \nabla_\Gamma^\varepsilon\, \psi |\nabla v| \, dV. \tag{28}$$

The construction of w_ε is complicated and described in detail in Section 4.2

Deriving a regularization for the fracture sources and sinks term $\int_\Gamma q_{fs}\psi \, dS$ using the phase-field function v would require some regularity on q_{fs}. In typical application, however, q_{fs} consists of a series of point sources $q_{fs}(x) = \sum_{i=1}^n Q_{f,i}\delta(x - x_i)$, x_i representing the location of the source or sink term, and Q_{f_i} the flow rate. We introduce the regularized source term

$$q_{fs}^\varepsilon(x) = \sum_{i=1}^n Q_{f,i}\delta_\varepsilon(x - x_i), \tag{29}$$

where $\delta_\varepsilon(x) := \frac{e^{-|x|}}{a_N \varepsilon^N}$, and a_N denotes the surface area of the unit sphere of dimension N, *i.e.* $a_2 = 2\pi$ and $a_3 = 4\pi$. Our phase-field approximation of the source/sink term is therefore

$$\int_\Gamma q_{fs}\psi \, dS \simeq \int_\Omega q_{fs}^\varepsilon \psi |\nabla v| \, dV. \tag{30}$$

The approximation of all remaining terms of (14) is straightforward, so that the phase-field approximation of our combined flow model in weak form becomes

$$\begin{aligned}&\int_\Omega v^2 \frac{\partial \zeta}{\partial t}\psi \, dV + \frac{K}{\mu}\int_\Omega \nabla p \cdot \nabla \psi \, dV + \int_\Omega \frac{w_\varepsilon^3}{12\mu}\nabla_\Gamma^\varepsilon p \cdot \nabla_\Gamma^\varepsilon \psi |\nabla v| \, dV \\ &\quad = \int_\Omega v^2 q_{rs}\psi \, dV - \int_{\partial_N \Omega} q_n \psi \, dV + \int_\Omega q_{fs}^\varepsilon \psi |\nabla v_\varepsilon| \, dV - \int_\Omega \psi \frac{\partial \vec{u}}{\partial t}\cdot \nabla v \, dV.\end{aligned} \tag{31}$$

4. Numerical implementation

We implemented our model consisting of the variational principle for crack evolution (26) coupled with fluid flow (31) using colocated bi-linear (for two dimensional models) and tri-linear (for three dimensional models) finite elements for $\vec{u}$, p, and v. For the sake of simplicity, our implementation is limited to structured grids. The linear algebra, constrained minimization and non-linear solvers are provided by PETSc [78,79]. The basis of our algorithm is an extension of the alternate minimizations originally introduced in [35]. At each time step, we alternate between solving for v for fixed $\vec{u}$ and p and solving for $\vec{u}$ and p satisfying static equilibrium and coupled flow equation (31), for fixed v. The former problem reduces to a box-constrained quadratic minimization problem, which can easily be reformulated as a variational inequality. Convergence for this step is measured by the difference between v values of consecutive fracture evolution steps. For the later, we extend the stress-split approach of [80] to account for the modified fluid flow problem. In this loop, the error is defined as the difference between consecutive values of a volume averaged pressure. A tolerance value of 1×10^{-4} is used to stop both solution steps.

4.1. Modified stress split

Substituting (8) into (31) and introducing the volumetric stress $\sigma_{vol} := \frac{1}{3}\mathrm{tr}\sigma = \kappa\nabla\cdot\vec{u} - \alpha p$, the first term in (31) becomes

$$\begin{aligned}\int_\Omega v^2\frac{\partial\zeta}{\partial t}\psi\,dV &= \int_\Omega v^2\frac{\partial}{\partial t}\left(\alpha\nabla\cdot\vec{u}+\frac{1}{M}p\right)\psi\,dV\\ &= \int_\Omega v^2\left(\frac{1}{M}+\frac{\alpha^2}{\kappa}\right)\frac{\partial p}{\partial t}\psi\,dV + \int_\Omega v^2\frac{\alpha}{\kappa}\frac{\partial\sigma_{vol}}{\partial t}\psi\,dV.\end{aligned} \tag{32}$$

Following the stress-split proposed in [80], the mean stress is evaluated with the previous iteration step's value ($\sigma_{vol} = \sigma_{vol}^k$) while the pressure with the current iteration ($p = p^{k+1}$). Thus substituting (32) into (31) then yields

$$\begin{aligned}&\int_\Omega v^2\left(\frac{1}{M}+\frac{\alpha^2}{\kappa}\right)\frac{\partial p^{k+1}}{\partial t}\psi\,dV + \frac{K}{\mu}\int_\Omega\nabla p^{k+1}\cdot\nabla\psi\,dV + \int_\Omega\frac{(w_\varepsilon^k)^3}{12\mu}\nabla_\Gamma^\varepsilon p^{k+1}\cdot\nabla_\Gamma^\varepsilon\psi|\nabla v|\,dV\\ &= \int_\Omega q_{rs}\psi\,dV - \int_{\partial_N\Omega} q_n\psi\,dV + \int_\Omega q_{fs}^\varepsilon\psi|\nabla v_\varepsilon|\,dV - \int_\Omega\psi\frac{\partial\vec{u}^k}{\partial t}\cdot\nabla v\,dV - \int_\Omega v^2\frac{\alpha}{\kappa}\frac{\partial\sigma_{vol}^k}{\partial t}\psi\,dV,\end{aligned} \tag{33}$$

where superscript k represents the iteration step. Because of the regularized variable, (33) still imposes an ill-conditioned system for $v = 0$. Here we propose a modification similar to the stress-splitting in [80,81] to improve the stability by using the Biot's compressibility $(1/M)$ as a stabilizing term in the following form:

$$\begin{aligned}&\int_\Omega\left(\frac{1}{M}+v^2\frac{\alpha^2}{\kappa}\right)\frac{\partial p^{k+1}}{\partial t}\psi\,dV + \frac{K}{\mu}\int_\Omega\nabla p^{k+1}\cdot\nabla\psi\,dV + \int_\Omega\frac{(w_\varepsilon^k)^3}{12\mu}\nabla_\Gamma^\varepsilon p^{k+1}\cdot\nabla_\Gamma^\varepsilon\psi|\nabla v|\,dV\\ &= \int_\Omega q_{rs}\psi\,dV - \int_{\partial_N\Omega} q_n\psi\,dV + \int_\Omega q_{fs}^\varepsilon\psi|\nabla v_\varepsilon|\,dV - \int_\Omega\psi\frac{\partial\vec{u}^k}{\partial t}\cdot\nabla v\,dV\\ &\quad - \int_\Omega v^2\frac{\alpha}{\kappa}\frac{\partial\sigma_{vol}^k}{\partial t}\psi\,dV + \int_\Omega\frac{1}{M}\left(1-v^2\right)\frac{\partial p^k}{\partial t}\psi\,dV.\end{aligned} \tag{34}$$

In solving (26) and (34), the equations are scaled to convert the system to a more numerically benign form (see Appendix for details about non-dimensionalization).

4.2. Computation of the fracture aperture

Reasoning as in Section 3.2 for (24), for almost every point $x \in \Gamma$, and almost every unit vector $\vec{\nu}$, we have that

$$w(x) := [\![\vec{u}(x)\cdot n_\Gamma]\!] \simeq \int_{\Omega^{x,\nu}}\vec{u}\cdot\nabla v\,dx,$$

where $\Omega^{x,\nu}$ denotes the one dimensional section of Ω through x in the direction $\vec{\nu}$.

For each cell e, if $\max_e v \geq 1-\delta_\varepsilon$, we set $w_\varepsilon(e) = 0$. We then integrate $\vec{u}\cdot\nabla v$ through the center of e along the streamline of ∇v over the segment $l_\varepsilon(e)$ by taking a discretized step $\triangle l_\varepsilon(e)$ where v is decreasing if moving towards the fracture and is increasing if moving away from it. Therefore, the line integration is performed twice at every cell in both descending ($s = -1$) and ascending ($s = 1$) directions of v by setting the search direction, s, accordingly. If the search crosses a fractured cell ($\vec{n}_{\Gamma,j+1}\cdot\vec{n}_{\Gamma,j} < 0$) then the search direction is flipped to the ascending direction ($s = 1$). If the search leaves the transition zone ($v \geq 1-\delta_\varepsilon$) or enters a transition zone by another fracture ($\vec{n}_{\Gamma,j+1}\cdot\vec{n}_{\Gamma,i} < 0$), then the integration is stopped (see Fig. 2). Detailed procedures are described in Algorithm 1.

Fig. 3 shows the computed aperture of a crack in an impermeable medium subject to a constant pressure for decreasing discretization size. An excellent match with the exact solution of [82] is obtained.

Fig. 4 shows the same computation for a slant crack. We notice that whereas along the fracture sides, the aperture computed using our algorithm is invariant by rigid motion, it is not the case near the crack tip (see how the aperture density does not vanish near the crack tip in Fig. 4-(right)).

This effect is easily understood by looking at the variations of ∇v along one dimensional sections as in Fig. 5. Away from the crack tip, the line average of ∇v along one-dimensional sections vanishes as $\varepsilon \to 0$, which is consistent with the construction of the near optimal phase-field in Γ–convergence recovery sequence as a function of the distance to the crack. Near crack tips, this is evidently not the case.

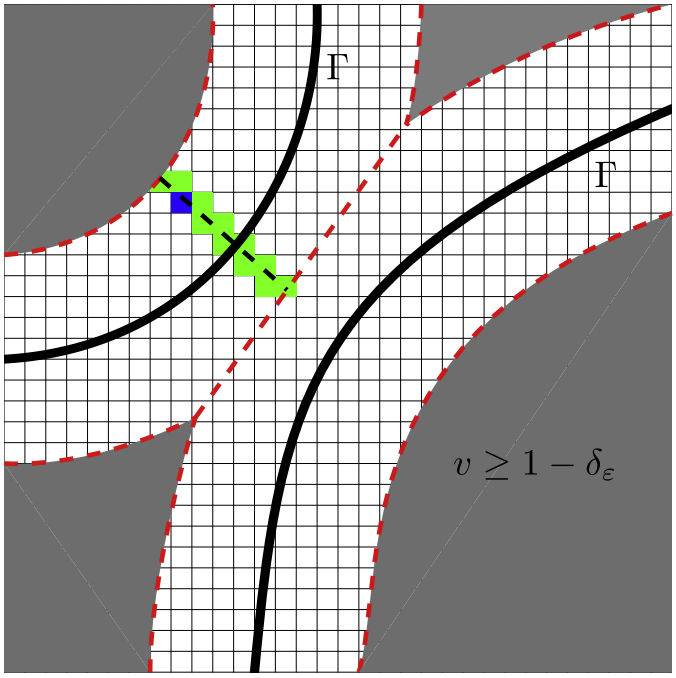

Fig. 2. Computation of w_ε. The grayed area is such that $v \geq 1 - \delta_\varepsilon$, so that $w_\varepsilon = 0$. The blue cell is the current cell, the line $l_\varepsilon(e)$ is the dashed black line and $w_\varepsilon(e) = \int_{l_\varepsilon(e)} \vec{u} \cdot \nabla v \, dx$. The green cells are components used for the line integral . (For interpretation of the references to color in this figure legend, the reader is referred to the web version of this article.)

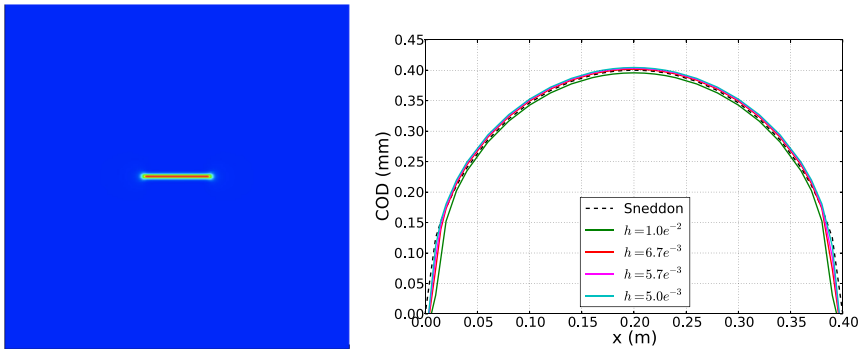

Fig. 3. Fracture width profile computed for a pressurized line crack in an impermeable medium. The plot labeled Sneddon is the analytical solution of the fracture width taken from [82]. (left): phase-field representation of the crack. (right): pressure profile along the crack compared to the exact solution for multiple mesh resolutions.

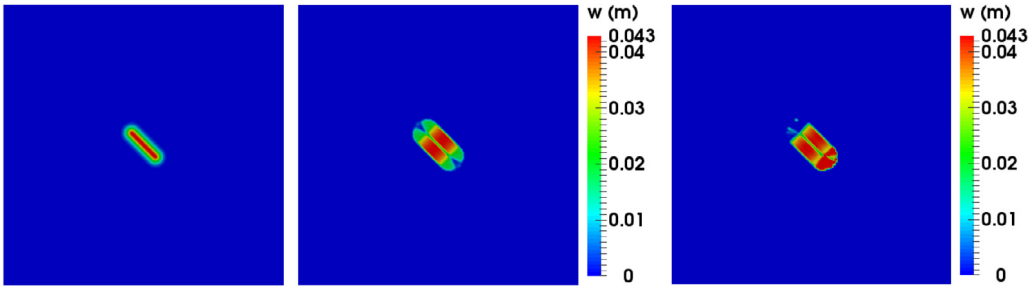

Fig. 4. Pressurized slant crack in an impermeable medium. (left): Phase-field description of the crack. (center): Computed regularized aperture. (right): Computed regularized aperture in the computational domain subject to a rigid body translation.

Algorithm 1 Fracture aperture opening computation at the element e_i

Let $v_i = v(e_i)$ and $\mathbf{x}_i$ be the centroid of element e_i
Set $j = i$, $\vec{n}_{\Gamma,i} = \nabla v_i/|\nabla v_i|$, and $s = 1$
repeat
    Let $\mathbf{x}_{j+1} := \mathbf{x}_j + s\triangle l_\varepsilon \vec{n}_{\Gamma,j}$.
    Find the element to which $\mathbf{x}_{i+1}$ belongs to and let $\vec{n}_{\Gamma,i+1} := \nabla v_{i+1}/|\nabla v_{i+1}|$
    if $\vec{n}_{\Gamma,j+1} = 0$ **then**
        $\vec{n}_{\Gamma,j+1} = \vec{n}_{\Gamma,j}$
    else if $\vec{n}_{\Gamma,j+1} \cdot \vec{n}_{\Gamma,j} < 0$ **then**
        $\vec{n}_{\Gamma,i} = -\vec{n}_{\Gamma,i}$
        $s := -s$
    $w := w + \triangle l_\varepsilon(\vec{u}_j \cdot \nabla v_j + \vec{u}_{j+1} \cdot \nabla v_{j+1})/2$
    $j := j + 1$
until $v_{j+1} \geq 1 - \delta_\varepsilon$ or $\vec{n}_{\Gamma,j+1} \cdot \vec{n}_{\Gamma,i} < 0$
Set $j = i$, $\vec{n}_{\Gamma,i} = -\nabla v_i/|\nabla v_i|$ and $s = -1$
repeat 4–12
until $v_{j+1} \geq 1 - \delta_\varepsilon$ or $\vec{n}_{\Gamma,j+1} \cdot \vec{n}_{\Gamma,i} < 0$

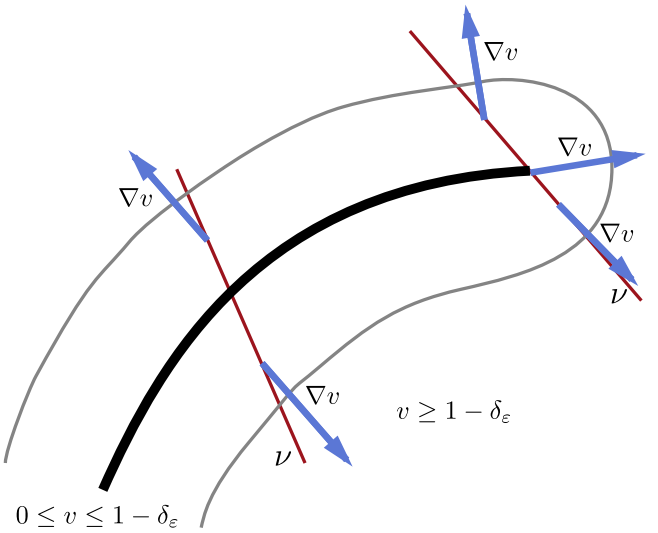

Fig. 5. Computation of the average of normal displacement across the fracture through one-dimensional section. Far from the crack tip, the one-sided averages of ∇v are a good approximation of $\vec{n}_\Gamma$, whereas near crack tips or kink, they are not.

We propose to mitigate this effect by introducing a small tolerance δ'_ε and constructing the tip indicator function

$$I_\varepsilon(e) := \begin{cases} 1 & \text{if } \left|\int_{l_\varepsilon(e)} \nabla v|\, dx\right| \leq \delta'_\varepsilon \\ 0 & \text{otherwise,} \end{cases} \tag{35}$$

which vanishes near the crack tips while taking the value 1 away from them and can be computed together with w_ε, at a very small cost. Our regularized aperture function is then simply given by $\tilde{w}_\varepsilon(e) := I_\varepsilon(e) w_\varepsilon(e)$. Note that when using the $\mathtt{AT}_1$ model for which the transition zone of the phase-field v is finite and equal to 2ε, δ'_ε can be made arbitrarily close to 0, or in practice of the order of the machine precision. Fig. 6 shows the indicator function I_ε and modified regularized aperture $\tilde{w}_\varepsilon$ for the crack pattern of Fig. 4-(right). We observe that the modified aperture density properly vanishes near the crack tips.

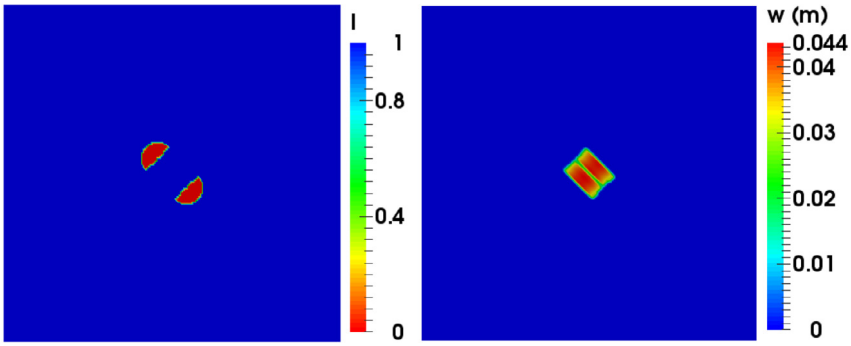

Fig. 6. Crack tip indicator function I_ε and (left): modified regularized aperture $\tilde{w}_\varepsilon$ for the crack pattern of 4 (right).

Table 1
Reservoir properties for verification of coupled hydraulic fracture model.

Parameter	Value
x	200 m
Δt	0.283 s
E	17 GPa
ν	0.2
G_c	100 Pa m
ϕ	0.2
α	1
K_s	10 GPa
K_f	0.625 GPa
μ	4×10^{-4} Pa s
Q_{fs}	5×10^{-4} m^2 s^{-1}

5. Numerical results

5.1. Verification: KGD hydraulic fracture propagation in the near K-regime

The developed numerical model is verified by solving the plane-strain fluid-driven fracture propagation problem, under the near K-regime defined in [61,83]. This regime is characterized by the constant injection of a low viscosity fluid with no leak-off from the fracture. Of course, as the name suggests, this fracturing regime is different from the K-region, and its deviation from the K-region solution is dependent on a dimensionless fluid viscosity, $\mathcal{M}$. The semi-analytical solution in [84] corrects for this deviation from the K-vertex, by providing good approximations for the time evolution of the fracture opening displacement, fracture length and fluid pressure as functions of $\mathcal{M}$,

$$\mathcal{M} = \frac{\mu' Q}{E'} \left(\frac{E'}{K'} \right)^4 \tag{36}$$

where $E' = \frac{E}{1-\nu^2}$, $\mu' = 12\mu$, and $K' = \sqrt{\frac{32\, G a_c E'}{\pi}}$.

The computational domain is a square of size 200 m $\times$ 200 m with an initial fracture of length $l_0 = 3$ m, inclined at 45° and centered in the domain as shown in Fig. 4-left. Fluid is injected into the center of the fracture at a constant rate of $Q = 5 \times 10^{-4}$ m^2 s^{-1}. The initial and boundary conditions are $p = 0$ and $\vec{u} = 0$. Table 1 show the values of reservoir, fluid and model parameters used for in this computation. All the properties are assumed homogeneous and isotropic where applicable.

First, we investigated the mesh sensitivity of the numerical model by running computations at three different mesh resolutions. The ratio of mesh resolution to phase field characteristic length scale was kept constant for all the computations (i.e. $\frac{\varepsilon}{h} = 4$). The results are shown in Fig. 7, where the dashed lines are the analytical solution for $\mathcal{M} \approx 0.0$. The linear component of the analytical solution is the actual pressure path prior to propagation for the

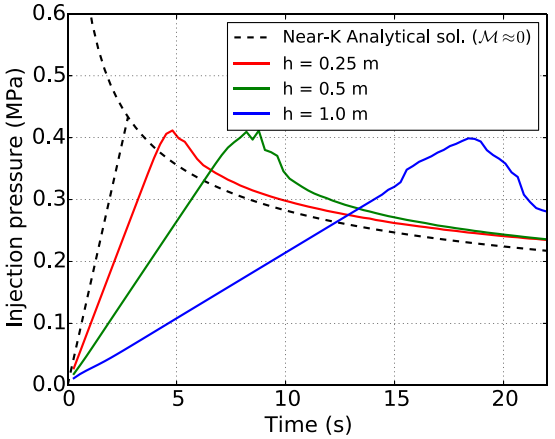

Fig. 7. Injection fluid pressure as a function of time, for different mesh resolutions.

given initial fracture length, while the curve is the critical pressure for all fracture lengths. As evident in the figure, our numerical solution approaches the analytical solution as the mesh resolution increases. A tolerance value of 1×10^{-4} was used for both the inner and outer loops of the algorithm. Although we imposed a combined maximum iteration of 101 for the inner and outer loops at each time step, the solution converged in about 20 iterations prior to fracture propagation and in over 60 iterations during fracture propagation time steps.

Using the mesh resolution of $h = 0.25$ m, we compare computations for $\mathcal{M} \approx 0.0$ and $\mathcal{M} \approx 0.041$. In order to replicate the near K-regime, very low reservoir permeability ($k = 2.83 \times 10^{-16}$ m^2) is used in the simulation. Fig. 8 compares the numerical results for injection fluid pressure, fracture half length and fracture mouth width for both cases of $\mathcal{M} \approx 0.0$ and $\mathcal{M} = 0.041$, with the analytical solution of [84]. As we prescribe an initial fracture, mismatch is observed in the early time until the initial crack is filled with fluid. Considering the various assumptions that have been made in the development of the regularized flow model and in the fracture width computation, the pressure and the width show fairly good comparisons between our numerical results and the analytical solutions while the computed length does not match as good as the others. The reason for this is that while the pressure and the width are explicitly computed, the length is extracted from the surface energy term which is influenced by the profile of the phase-field variable and is overestimated due to the profile around the tip [85,86]. One observes that $\mathcal{M} = 0.041$ results in a higher injection pressure and fracture mouth aperture and shorter fracture length than those obtained for $\mathcal{M} \approx 0$.

5.2. *Effect of reservoir permeability on fracture propagation in the near K-regime*

In the previous section, we verified the model by simulating hydraulic fracture propagation characterized by very low fluid viscosity and reservoir permeability. Here we investigate the effect of increasing reservoir permeability on hydraulic fracture propagation in the same regime. Specifically, we compare numerical results for fluid pressure, fracture geometry and propagation direction with the analytical results for the $K-$regime. The computational domain is the same as in Fig. 4-left but with $k = 2.8 \times 10^{-15}$ m^2, 5.7×10^{-15} m^2, 1.1×10^{-14} m^2, 1.7×10^{-14} m^2 and 2.3×10^{-14} m^2 respectively, and other parameters are the same as in Table 1.

Fig. 9 compares the numerical injection pressure, change in fracture half length, fracture mouth aperture and fracture volume with those of the toughness dominated regime derived from Sneddon's analytical solution [46]. One observes that the critical pressures are not significantly affected by reservoir permeability for the low fluid viscosity. However, increasing reservoir permeability delays the onset of fracture propagation due to increasing fluid loss to the surrounding reservoir. Correspondingly, the fracture propagation rate is slower as reservoir permeability increases. In addition, the large fluid loss experienced in higher permeability computations leads to smaller fracture mouth opening displacement and fracture volumes respectively. For all the quantities plotted, the deviation of the numerical results from the analytical solutions ($\mathcal{M} = 0$) increases as reservoir permeability increases. This is so since the fracture propagation regime changes from storage dominated to leak-off dominated.

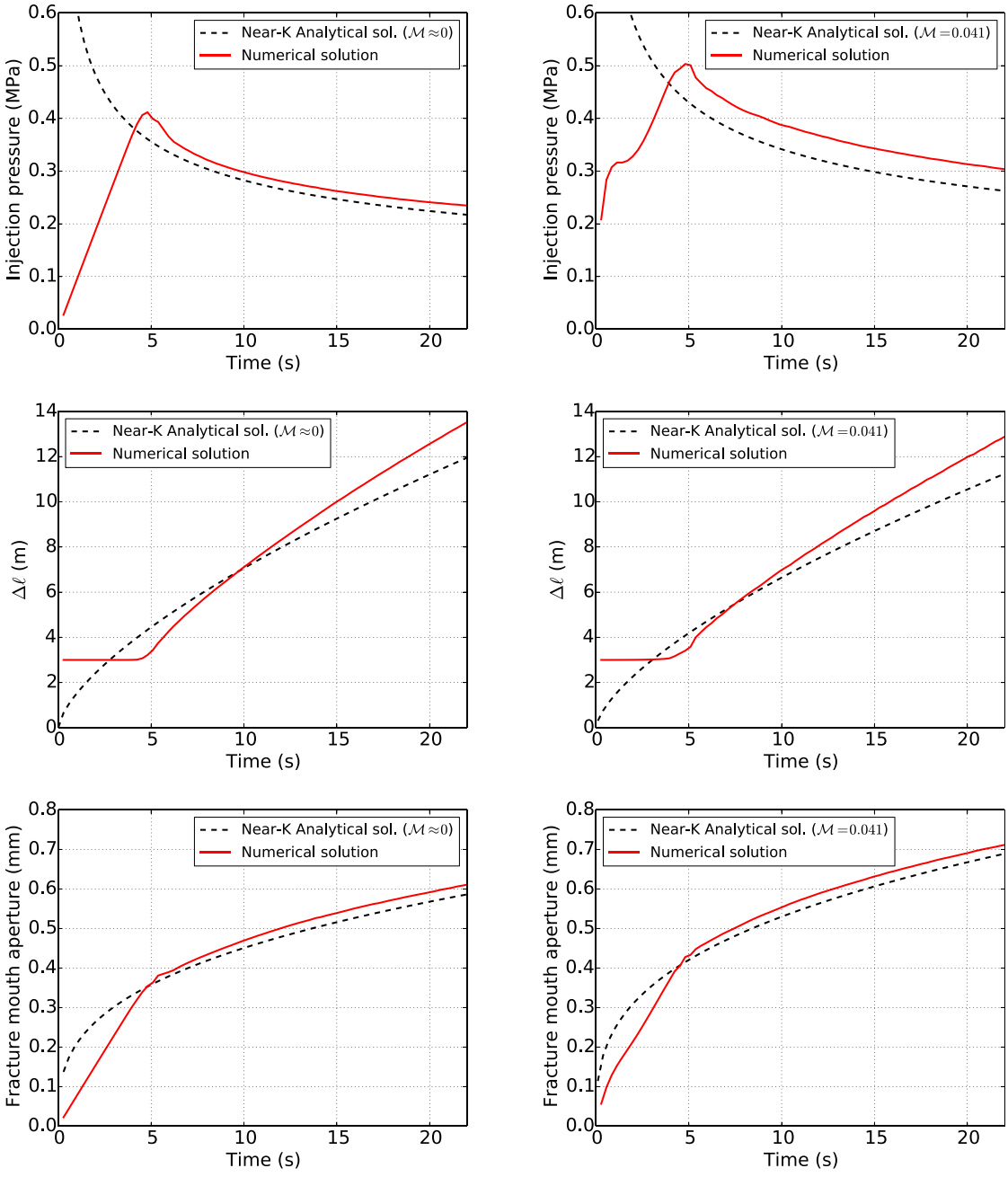

Fig. 8. KGD injection fluid pressure for toughness dominated propagation regime.

In another set of numerical computations, we study the effect of directional variation in reservoir permeability on fracture propagation directions. Anisotropy in reservoir permeability is created by keeping k_z constant at 2.8×10^{-15} m^2 and varying k_x. The numerical results for fracture propagation are shown in Fig. 10, for $k_x = 5.7 \times 10^{-13}$ m^2, 2.3×10^{-13} m^2, 1.1×10^{-13} m^2 and 5.7×10^{-14} m^2 respectively. As propagation initiates, the fracture kinks for anisotropic permeability ratio (k_x/k_z) greater than 10. The change in propagation direction occurs as the fracture seeks the direction that offers the least resistance to fluid flow, which in this case is the horizontal direction $(k_x > k_z)$. The kinking angle also increases with increasing k_x/k_z.

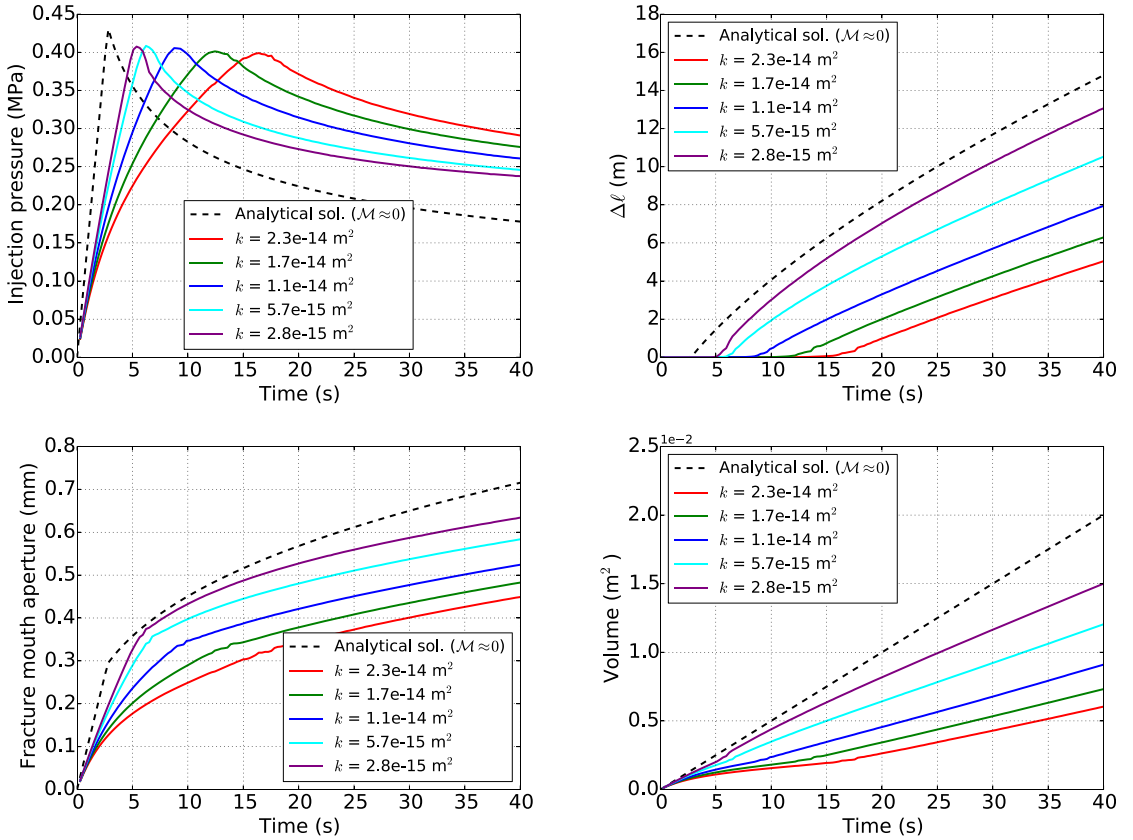

Fig. 9. Plots of fracturing injection pressure, change in fracture length, fracture mouth aperture and fracture volume for different reservoir permeabilities.

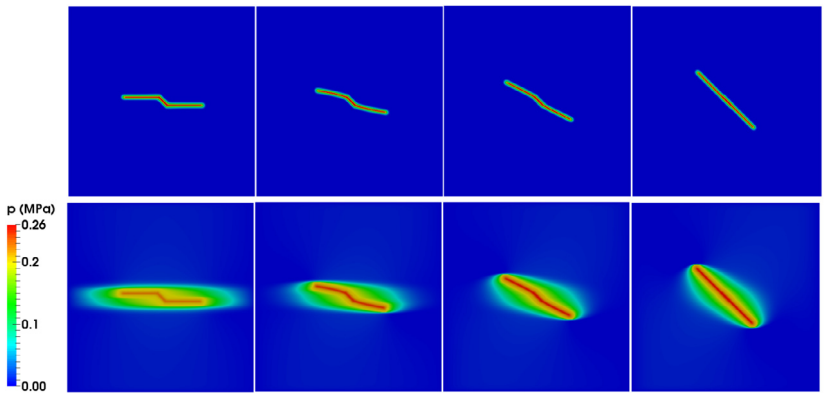

Fig. 10. Effect of reservoir permeability anisotropy on fracture propagation patterns. The top and bottom rows show snap shots of the fractures and pressure distributions in the computational domains. Plots from left to the right columns are for $k_x = 5.66 \times 10^{-15}$ m^2, 2.26×10^{-15} m^2, 1.13×10^{-15} m^2 and 0.57×10^{-15} m^2 respectively.

5.3. Well shut-in after fracture propagation

In a minifrac test performed in the petroleum industry, after the initial fractures are created and extended, the injection well will be shut-in. During the shut-in period, fluid pressure decline occurs because the fluid flows back into the well or leaks-off into the adjoining reservoir. To mimic the minifrac test, we perform numerical experiments by

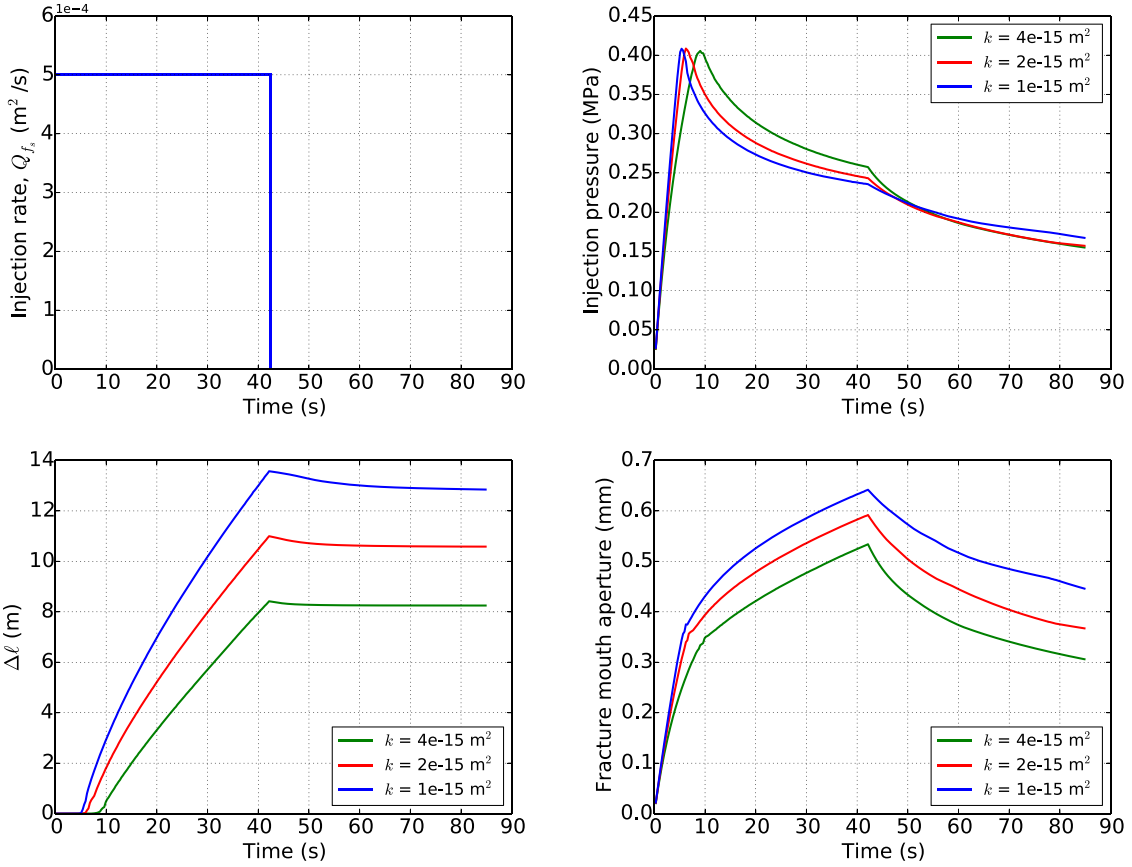

Fig. 11. Change in fracture length and fracture mouth aperture during well shut-in operation for different reservoir permeabilities. The well is shut-in after 42 s. (top-left) Injection rate as a function of time. (top-right) Injection pressure as a function of time. (bottom-left) Change in fracture half length. (bottom-right) Fracture mouth aperture.

shutting-in the well after a period of fluid injection and fracture propagation. The fluid pressure and fracture geometry changes are analyzed before and after the well shut-in. The reservoir model and initial fracture geometry are the same as in Section 5.2. Fluid viscosity is $\mu = 1 \times 10^{-4}$ Pa s while other parameters are the same as in Table 1. Three different reservoir permeabilities of $k = 4 \times 10^{-15}$, 2×10^{-15}, and 1×10^{-15} m^2 are considered. Fluid is injected into the fracture at a constant rate of $Q_{fs} = 5 \times 10^{-2}$ m s^{-1} for 42 s, after which the well is shut-in. The numerical results for fluid injection with well shut-in are shown in Fig. 11 while results without well shut-in are those in Fig. 9. The pressure responses are such that after fluid injection stops at 42 s, pressure decline increases as fluid leaks-off into the reservoir. The rate of this decline is directly proportional to the reservoir permeability. Similarly, fracture mouth aperture decreases with declining fluid pressure. The fracture length remains constants after well shut-in, since fluid pressure falls below the critical value necessary for continued fracture propagation. Fig. 12 shows the evolution of fluid pressure in the reservoir at different times for $k = 4 \times 10^{-15}$ m^2. The fracture length increases until t = 42 s and remains constant thereafter. Fluid leak-off into the reservoir is highlighted by the decreasing pressure inside the fracture and increasing fluid diffusion into the reservoir as time progresses beyond the well shut-in time.

5.4. Hydraulic fracture propagation in layered reservoirs

Three dimensional computations are carried out to highlight the role of varying mechanical properties of reservoir layers on hydraulic fracture height growth. Fig. 13 shows the computational geometry with the initial penny-shaped fracture in the middle of the domain. The reservoir is a cube of size 50 m × 50 m × 50 m while the initial fracture has a radius of 5 m. Inviscid fracturing fluid ($\mu = 4 \times 10^{-7}$ Pa s) is injected into the center of the fracture. The reservoir is

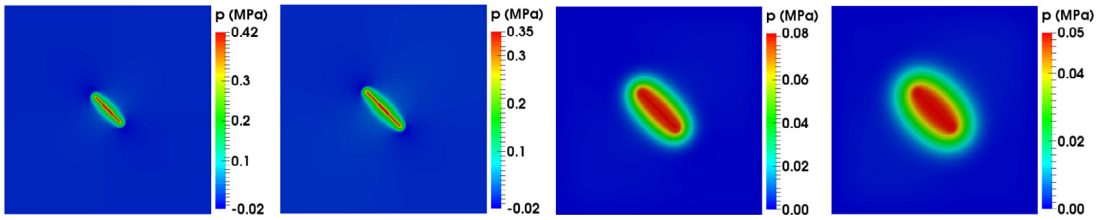

Fig. 12. Snap shots of pressure distribution in the reservoir with $k = 4 \times 10^{-15}$ m^2 at times $t = 144$, 175, 1416, and 2826 s. The well is shut-in after 42 s.

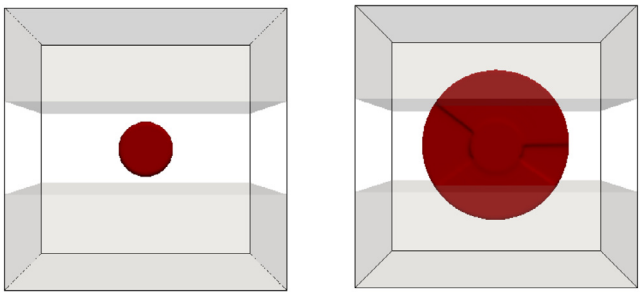

Fig. 13. Penny shaped fracture in a three dimensional reservoir with 3 layers. Fracture shape is taken as the contour at $v = 0.1$. The layers are identified by different colors. Top and bottom layers have the same properties, hence the same color representation.

Table 2
Reservoir properties for fracture propagation in a three layered, three dimensional reservoir.

Parameter	Value
x	50 m
Δt	0.14 s
E	17 GPa
v	0.2
G_c	100 Pa m
k	2.83×10^{-13} m^2
ϕ	0.2
α	1
K_s	2 GPa
K_f	0.125 GPa
μ	4×10^{-7} Pa s
Q_{fs}	5×10^{-2} m^2 s^{-1}

divided into three vertical layers with interfaces at 17 m and 25 m respectively. This means that the fracture is located in the middle layer and is perpendicular to the interfaces. We assume that both top and bottom layers are similar, with the same values for reservoir properties as highlighted by the color contrast in Fig. 13. Layering in the reservoir is created by varying the values of either E, G_c or k between the layers while the other properties are the same for all the layers. The base reservoir properties for all the layers are as in Table 2. Our numerical results for fracture propagation in the reservoir with uniform properties (base values) in all layers are shown in Fig. 13 and obviously, the penny shape is unchanged throughout the propagation of the fracture.

Results for fractures propagation in reservoir with varying G_c between the layers are shown in Fig. 14. Higher fracture toughness of the external layers favors hydraulic fracture growth within the middle layer. Under these conditions, the fracture extends more in length than in height. In fact, for very high $\frac{G_{c,\text{ext}}}{G_{c,\text{mid}}}$ ratio, the fracture is completely confined in the middle layer as seen in Fig. 14c. As a result, the height is constant, approximately equal to the thickness of the middle layer. On the other hand, a reduction in $\frac{G_{c,\text{ext}}}{G_{c,\text{mid}}}$ favors fracture growth into the top and bottom layer, with a geometry that is longer in the vertical direction than in the horizontal direction.

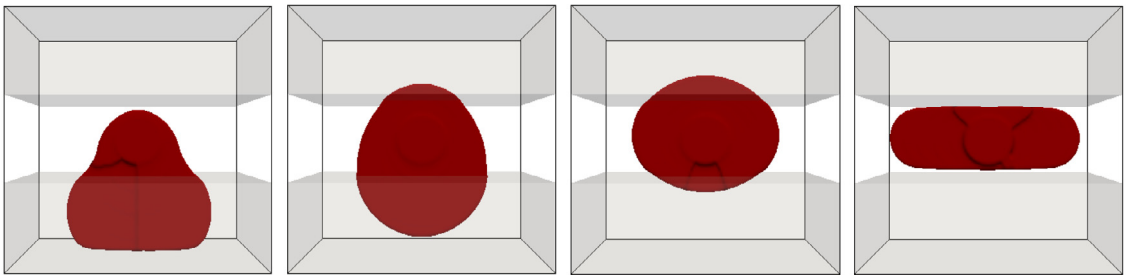

Fig. 14. Propagated hydraulic fracture in a three layers reservoir with different fracture toughness. (left to right): $\frac{G_{c,\text{ext}}}{G_{c,\text{mid}}} = 0.7$, 0.9, 1.2, and 10.

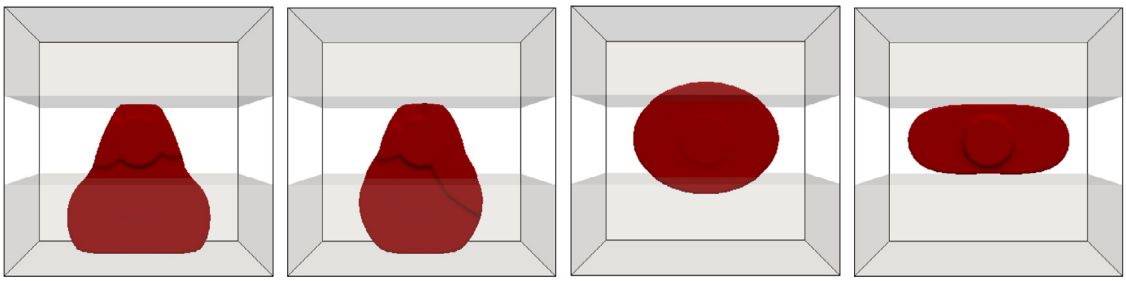

Fig. 15. Propagated hydraulic fracture in a three layers reservoir with different Young's modulus. (left to right): $\frac{E_{\text{ext}}}{E_{\text{mid}}} = 0.1$, 0.2, 2, and 5.

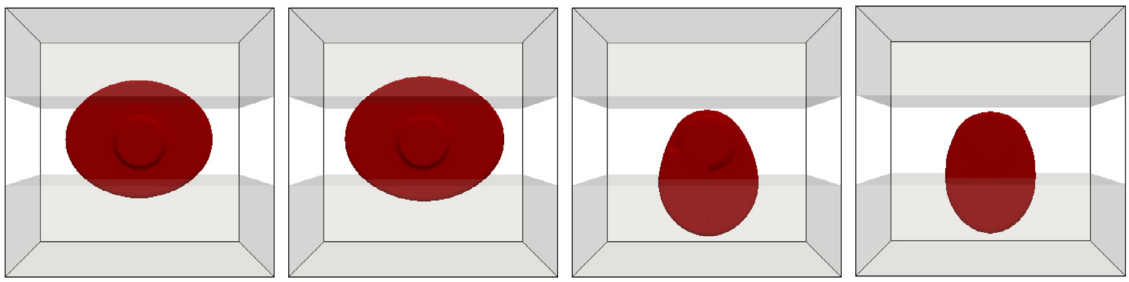

Fig. 16. Propagated hydraulic fracture in a three-layered reservoir with permeabilities. (left to right): $k_{\text{ext}} = 2.83 \times 10^{-15}$ m^2 and $k_{\text{mid}} = 2.83 \times 10^{-17}$ m^2, $k_{\text{ext}} = 2.26 \times 10^{-15}$ m^2 and $k_{\text{mid}} = 2.83 \times 10^{-17}$ m^2, $k_{\text{ext}} = 2.83 \times 10^{-15}$ m^2 and $k_{\text{mid}} = 1.70 \times 10^{-15}$ m^2, and $k_{\text{ext}} = 2.83 \times 10^{-17}$ m^2 and $k_{\text{mid}} = 2.83 \times 10^{-15}$ m^2.

Fig. 15 shows the propagated hydraulic fracture geometries in the layered reservoir for different Young's modulus. Higher Young's modulus in the surrounding layers impedes fracture growth out of the middle layer while lower modulus in the surrounding layers encourages fracture growth out of the middle layer.

Lastly, the effect of varying reservoir permeability in the layered reservoir on the fracture geometry is shown in Fig. 16. For higher permeability in the middle layer, the fracture propagates more in the vertical direction than in the horizontal direction. On the other hand, lower permeability in the middle encourages fracture propagation in that layer with less extension in the vertical direction. As a result, the fracture has a higher length compared to its height.

We observe non-symmetric propagation in the combination of reservoir properties that otherwise would have favored uniform and equal propagation into the external layers, as in Figs. 14a, 14b, 15a, 15b, 16c and 16d. In these figures, the fracture extends more into the bottom layer than into the top layer. The evolution of these fractures is such that propagation is symmetric prior to reaching the boundary interfaces. However, due to floating point errors, the bottom part of the fracture reaches the lower interface before the top part reaches the top layer interface. Subsequent fluid injection favors fracture growth into the bottom layer. Although this geometry could have been reversed to favor growth into the top layer, the results indicate that it may be difficult to control hydraulic fracture growth in conditions

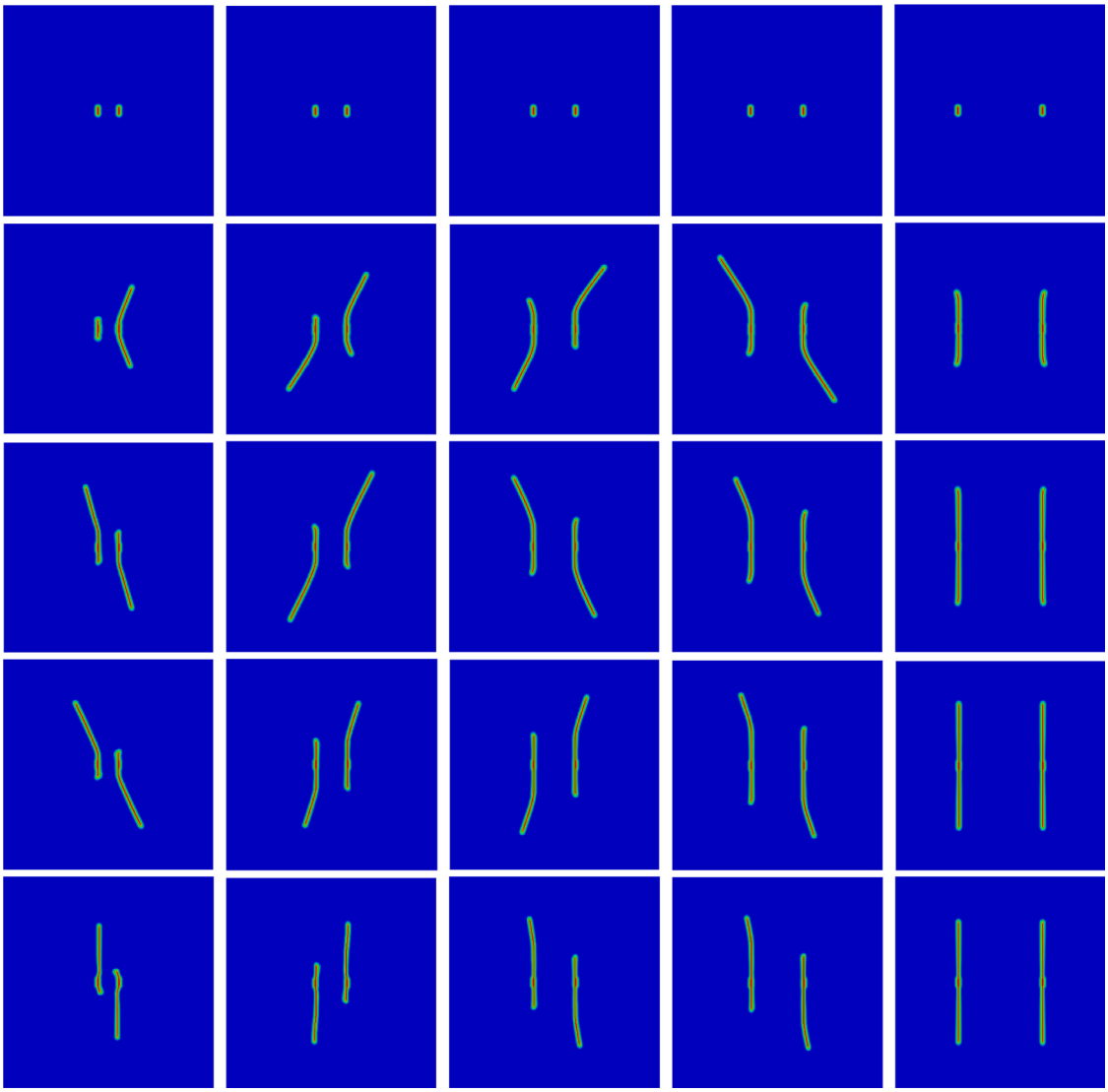

Fig. 17. Propagation of two pre-existing fractures with injection wells in the center of both fractures. The columns are for an initial fracture spacing of 20, 30, 40, 50, and 80 m respectively. The rows are for $k = 1.70 \times 10^{-14}$, 5.66×10^{-15}, 2.83×10^{-15}, and 1.41×10^{-15} m^2 respectively.

where fractures propagate into layers with lower resistance to fluid flow and rock deformation and subtle differences such as rock property can trigger asymmetric fracture growth at least in the toughness dominated region.

5.5. Propagation of multiple fractures

One of the unique features of our developed model is the ease in simulating propagation of multiple hydraulic fractures. Three cases containing, two, three and four initial fractures are considered to highlight this capability. In the first example, the two initial vertical fractures have half lengths of $l_0 = 3$ m and are both centrally located in a reservoir of size 200 m $\times$ 200 m. Four different fracture spacings are considered (20 m, 30 m, 40 m, 50 m and 80 m) and for each spacing, the reservoir permeability is also varied. For this problem, $K_s = 2$ GPa, $K_f = 0.125$ GPa and $\mu = 1 \times 10^{-5}$ Pa s while the other parameters are as in Table 1. Fluid is injected in the center of both fractures at equal rates of $Q_{fs} = 5 \times 10^{-4}$ m^2 s^{-1}. The first row in Fig. 17 is the phase-field representation of the initial fractures at different fracture spacings. Subsequent rows in the same figure are simulated results for increasing reservoir permeability.

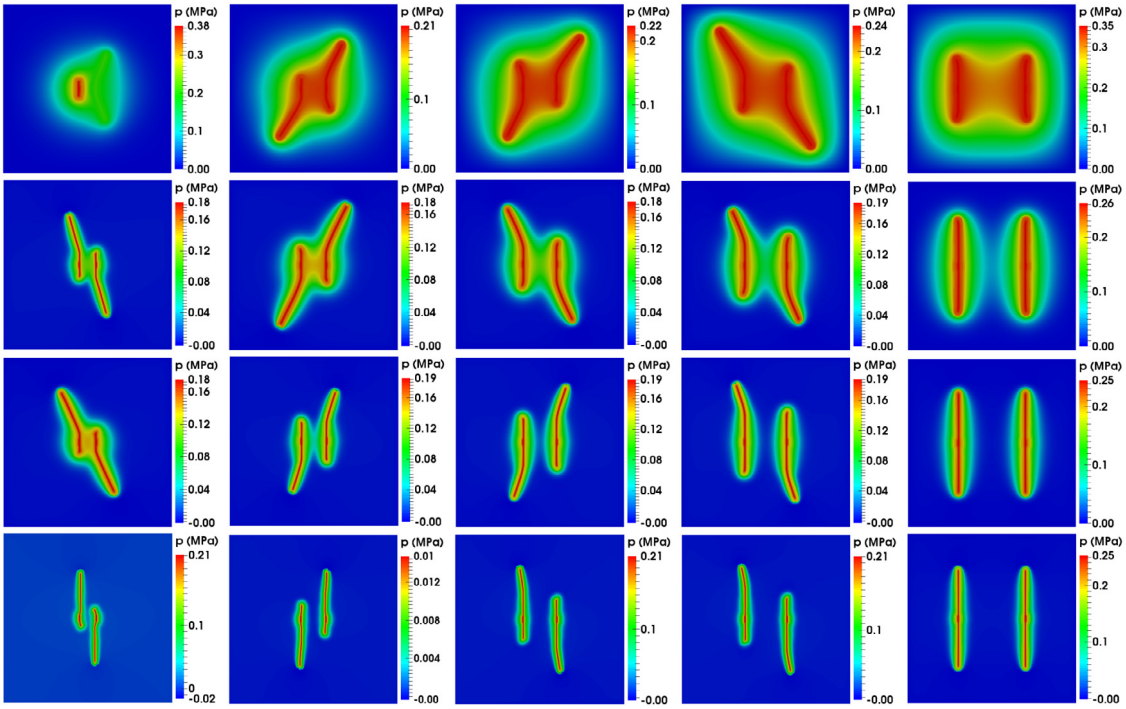

Fig. 18. Computed fluid pressure for fractures in Fig. 17. The columns are for an initial fracture spacing of 20, 30, 40, 50, and 80 m respectively. The rows are for $k = 1.70 \times 10^{-14}$, 5.66×10^{-15}, 2.83×10^{-15}, and 1.41×10^{-15} m^2 respectively.

Stress shadow effect is evident in all the computations as the fractures interact by propagating away from each other along curved paths. With increasing fracture spacing, the curvature of propagation reduces. Comparing the patterns from top to bottom for each column, one observes that decreasing reservoir permeability reduces fracture curvature and complexity. The computed fluid pressures are shown in Fig. 18.

Note that some of our numerical solutions are non-symmetric, which is consistent with the stability analysis in [85,86]. Loosely speaking symmetric crack patterns are critical points of the fracture energy, but become more and more unstable when pre-existing cracks become closer. In this case, a minimization-based model will naturally bifurcate towards one possibly non-symmetric realization of a family of stable fracture patterns.

Simulation results for the propagation of three and four initial fractures are also presented. Initial fracture half-lengths are 10 m and 3 m for the three and four fracture cases respectively. Both examples use a fracture spacing of 35 m and $k = 2.83 \times 10^{-15}$ m^2. Fig. 19 highlights the evolution of the fractures while Fig. 20 shows the corresponding fluid pressure distribution in the reservoir. For both examples, at early times, the external fractures grow faster than those in the center of the configuration. As the outer fractures propagate, they exert compressive stresses on the centrally located fractures. The compressive stresses oppose the growth of the internal fractures, leading to fluid pressure build up in the compressed fractures, as can be seen in the two middle columns of Fig. 20. However, with continuous fluid injection, the fluid pressure in the middle fractures builds up enough to eventually overcome the opposing compressive stress exerted on them. Rapid fracture growth is experienced and the final patterns seen on the right column of Fig. 19 are obtained.

6. Conclusions

In this paper, a unified fracture–porous medium flow model, which is regularized with a phase-field variable, is derived and coupled with the variational phase-field fracture model for simulation of hydraulic fracture propagation in poroelastic media. The fracture width and its cube are the primary links between the fracture fluid flow and deformation, and our approaches to approximate these explicit quantities are described in detail. The phase-field fracture representation technique, which is the foundation of the variational model, reduces computational cost and

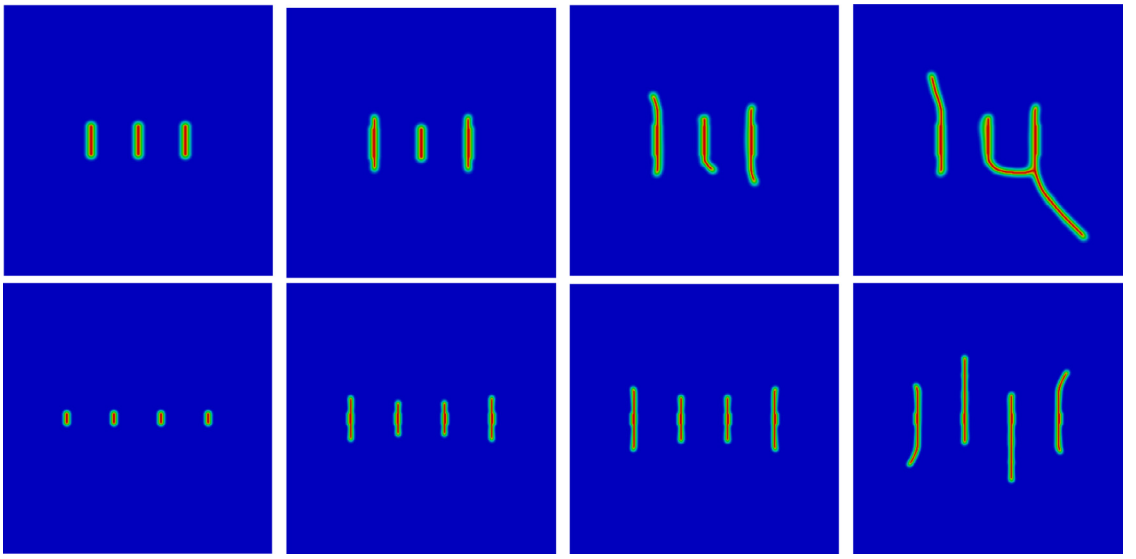

Fig. 19. Evolution of propagation paths for three and four parallel fractures with fluid injection into the center of each fracture. The top row are snapshots of the v-field for three fractures at 28.3, 570, 846, and 990 s. The bottom row shows snapshots of the v-field for four fractures at 7.1, 282, 354, and 426 s.

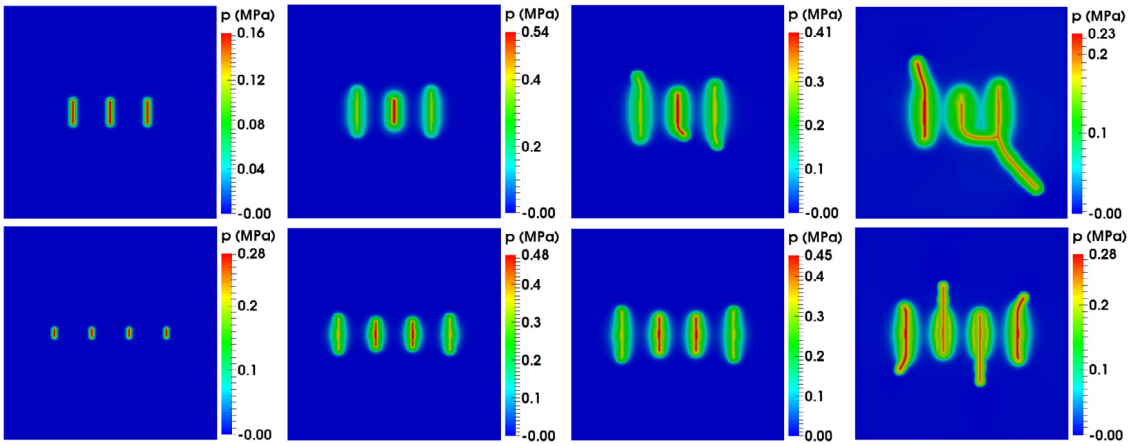

Fig. 20. Reservoir fluid pressure during the evolution of propagation paths for three and four parallel fractures with fluid injection into the center of each fracture. Top row is snapshot of the pressure distribution during evolution of the three fractures at 28.3, 570, 846, and 990 s. Bottom row is the snapshot of the pressure distribution during evolution of the four fractures at 7.1, 282, 354, and 426 s.

places no constraints on the complexity of fracture behavior and interactions. In contrast to existing models that utilize additional indicator function or level-set variables to distinguish the fracture and the porous medium domains, our model is unified with a single phase-field variable which regularizes both mechanical and flow equations without need for ad-hoc assumptions about extra parameters.

The numerical model was verified against the plane-strain (KGD) fracture near the toughness dominated regime and then applied to study the effect of reservoir parameters and fluid properties on fracturing fluid pressure, fracture geometries (length, height, width, radius) and fracture propagation paths. In addition to showing the applicability of the method in highlighting the effect of reservoir and fluid properties on KGD fracture propagation, other numerical examples also illustrate the ability of the method to simulate multiple fracture propagations and three dimensional fracture height growth in layered reservoirs. Stress shadow effect was found to influence the interaction between multiple fractures during propagation and decrease with increasing spacing between fractures (or with decreasing

permeability of the reservoir). For penny-shaped fracture propagation in reservoirs with varying properties between layers, numerical results demonstrate that the variational based energy minimization approach can indeed simulate the confinement or the breach of fractures into layers with lower resistance to fluid flow and rock deformation.

Acknowledgments

The authors are grateful to Chevron Energy Technology Company for the sponsorship of this research. Part of this material is based upon work supported by the National Science Foundation under Grant DMS-1312739 and DMS-0909267. Portions of this research were conducted with high performance computational resources provided by Louisiana State University (http://www.hpc.lsu.edu). This work used the Extreme Science and Engineering Discovery Environment (XSEDE) at Texas Center for Advanced Computing, which is supported by National Science Foundation grant number ACI-1548562 through allocation TG-DMS060014.

Appendix

Solving (26) and (31) can pose some numerical instability when realistic properties are assigned. By denoting scaled parameters with $\tilde{(\cdot)}$ and scaling factors with subscript o, following four input parameters are scaled to numerically favorable values (e.g. 1.0):

$$E = E_o\tilde{E}, \quad G_c = G_{co}\tilde{G}_c, \quad x = x_o\tilde{x}, \quad Q = Q_o\tilde{Q}. \tag{37}$$

Similarly other computed mechanical parameters are scaled as

$$\vec{u} = u_o\vec{\tilde{u}}, \quad p = p_o\tilde{p}, \quad \kappa = \kappa_o\tilde{\kappa}, \quad \mathbf{A} = E_o\tilde{\mathbf{A}}, \quad \vec{f} = f_o\vec{\tilde{f}}, \quad \vec{\tau} = p_o\vec{\tilde{\tau}}, \tag{38}$$

and the fluid flow related parameters as

$$w = u_o\tilde{w}, \quad M = E_o\tilde{M}, \quad \mu = \mu_o\tilde{\mu}, \quad K = k_o\tilde{K}, \quad t = t_o\tilde{t}. \tag{39}$$

In addition, the phase-field regularization parameter ε is represented as

$$\varepsilon = x_o\tilde{\varepsilon} \tag{40}$$

Substituting (37), (38), and (40) into (26) gives

$$\begin{aligned}\mathcal{F}_\varepsilon(\vec{u}, v; p) = {} & E_o x_o^{N-2} u_o \int_{\tilde{\Omega}} \tfrac{1}{2}\tilde{\mathbf{A}}\left(\mathrm{ve}(\vec{\tilde{u}}) - \frac{p_o x_o}{E_o u_o}\frac{\alpha\tilde{p}}{N\tilde{\kappa}}\mathrm{I}\right)\cdot\left(\mathrm{ve}(\vec{\tilde{u}}) - \frac{p_o x_o}{E_o u_o}\frac{\alpha\tilde{p}}{N\tilde{\kappa}}\mathrm{I}\right) d\tilde{V} \\ & - p_o u_o x_o^{N-1}\int_{\partial_N\tilde{\Omega}} \vec{\tilde{\tau}}\cdot\vec{\tilde{u}}\, d\tilde{S} - f_o u_o x_o^N \int_{\tilde{\Omega}} \vec{\tilde{f}}\cdot\vec{\tilde{u}}\, d\tilde{V} + p_o u_o x_o^{N-1}\int_{\tilde{\Omega}} \tilde{p}\,\vec{\tilde{u}}\cdot\tilde{\nabla} v\, d\tilde{V} \\ & + \frac{G_{co}\tilde{G}_c x_o^{N-1}}{4c_n}\int_{\tilde{\Omega}}\left(\frac{(1-v)^n}{\tilde{\varepsilon}} + \tilde{\varepsilon}|\tilde{\nabla} v|^2\right) d\tilde{V}.\end{aligned} \tag{41}$$

Dividing both sides by $E_o u_o^2 x_o^{N-2}$ and setting

$$u_o = \sqrt{\frac{G_{co}x_o}{E_o}}, \tag{42}$$

$$p_o = \sqrt{\frac{G_{co}E_o}{x_o}}, \tag{43}$$

lead to a more numerically favorable form:

$$\begin{aligned}\mathcal{F}_\varepsilon(\vec{\tilde{u}}, v; \tilde{p}) = {} & \int_{\tilde{\Omega}} \tfrac{1}{2}\tilde{\mathbf{A}}\left(\mathrm{ve}(\vec{\tilde{u}}) - \frac{\alpha\tilde{p}}{N\tilde{\kappa}}\mathrm{I}\right)\cdot\left(\mathrm{ve}(\vec{\tilde{u}}) - \frac{\alpha\tilde{p}}{N\tilde{\kappa}}\mathrm{I}\right) d\tilde{V} - \int_{\partial_N\tilde{\Omega}} \vec{\tilde{\tau}}\cdot\vec{\tilde{u}}\, d\tilde{S} - \int_{\tilde{\Omega}} \vec{\tilde{f}}\cdot\vec{\tilde{u}}\, d\tilde{V} \\ & + \int_{\tilde{\Omega}} \tilde{p}\,\vec{\tilde{u}}\cdot\tilde{\nabla} v\, d\tilde{V} + \frac{\tilde{G}_c}{4c_n}\int_{\tilde{\Omega}}\left(\frac{(1-v)^n}{\tilde{\varepsilon}} + \tilde{\varepsilon}|\tilde{\nabla} v|^2\right) d\tilde{V},\end{aligned} \tag{44}$$

where $\mathcal{F}_\varepsilon(\vec{\tilde{u}}, v; \tilde{p}) = \frac{1}{E_o u_o^2 x_o^{N-2}}\mathcal{F}_\varepsilon(\vec{u}, v; p)$.

For (34), we can similarly set

$$t_o = \sqrt{\frac{G_{co} x_o^{N-1}}{E_o Q_o^2}}, \tag{45}$$

$$\mu_o = \frac{G_{co}^2 x_o^{N-2}}{E_o Q_o}, \tag{46}$$

$$k_o = \frac{u_o^3}{x_o}, \tag{47}$$

$$m_o = E_o, \tag{48}$$

and (34) becomes

$$\begin{aligned}
&\int_{\tilde{\Omega}} \left(\frac{1}{\tilde{M}} + v^2 \frac{\alpha^2}{\tilde{\kappa}} \right) \frac{\partial \tilde{p}^{k+1}}{\partial \tilde{t}} \psi \, d\tilde{V} + \frac{\tilde{K}}{\tilde{\mu}} \int_{\tilde{\Omega}} \tilde{\nabla} \tilde{p}^{k+1} \cdot \tilde{\nabla} \psi \, dV + \int_{\Omega} \frac{(\tilde{w}_\varepsilon^k)^3}{12\tilde{\mu}} \tilde{\nabla}_\Gamma^\varepsilon p^{k+1} \cdot \tilde{\nabla}_\Gamma^\varepsilon \psi |\tilde{\nabla} v| \, dV \\
&= \int_{\Omega} \tilde{q}_{rs} \psi \, d\tilde{V} - \int_{\partial_N \tilde{\Omega}} \tilde{q}_n \psi \, d\tilde{V} + \int_{\tilde{\Omega}} \tilde{q}_{fs}^\varepsilon \psi |\tilde{\nabla} v| \, d\tilde{V} - \int_{\tilde{\Omega}} \psi \frac{\partial \vec{\tilde{u}}^k}{\partial \tilde{t}} \cdot \tilde{\nabla} v \, d\tilde{V} \\
&\quad - \int_{\tilde{\Omega}} v^2 \frac{\alpha}{\tilde{\kappa}} \frac{\partial \tilde{\sigma}_{vol}^{\,k}}{\partial \tilde{t}} \psi \, d\tilde{V} + \int_{\tilde{\Omega}} \frac{1}{\tilde{M}} (1 - v^2) \frac{\partial \tilde{p}^k}{\partial \tilde{t}} \psi \, d\tilde{V}.
\end{aligned} \tag{49}$$

In all the analyses, scaled Eqs. (44) and (49) were solved and the resulting variables were scaled back accordingly. We should note, however, that the dimensionless viscosity parameter introduced in (36) can now be expressed with the dimensionless parameters as:

$$\mathcal{M} = \frac{\mu_o Q_o E_o}{G_{co}} \frac{\tilde{\mu}' \tilde{Q}}{\tilde{E}'} \left(\frac{\tilde{E}'}{\tilde{K}'} \right)^4 = x_o^{N-2} \frac{\tilde{\mu}' \tilde{Q}}{\tilde{E}'} \left(\frac{\tilde{E}'}{\tilde{K}'} \right)^4.$$

For the line fracture problem, $N = 2$, it becomes

$$\mathcal{M} = \frac{\tilde{\mu}' \tilde{Q}}{\tilde{E}'} \left(\frac{\tilde{E}'}{\tilde{K}'} \right)^4. \tag{50}$$

Therefore, the dimensionless viscosity parameter is identical in the dimensionless space.

References

[1] D.A. Spencer, D.L. Turcotte, Magma-driven propagation of cracks, J. Geophys. Res 90 (1985) 575–580.

[2] J.R. Lister, R.C. Kerr, Fluid-mechanical models of crack propagation and their application to magma transport in dykes, J. Geophys. Res. 96 (B6) (1991) 10049.

[3] L.C. Murdoch, W.W. Slack, Forms of hydraulic fractures in shallow fine-grained formations, J. Geotech. Geoenvironment. 128 (6) (2002) 479–487.

[4] L. Johnson, P. Marschall, P. Zuidema, P. Gribi, Effects of post-disposal gas generation in a repository for spent fuel, high-level waste and long-lived intermediate level waste sited in opalinus clay, in: Technical repor, National Cooperative for the Disposal of Radioactive Waste (NAGRA), 2004.

[5] W. Minkley, D. Brückner, C. Lüdeling, Tightness of salt rocks and fluid percolation, in: 45. Geomechanik-Kolloqium, 2016.

[6] L. Jiang, A. Sainoki, H.S. Mitri, N. Ma, H. Liu, Z. Hao, Influence of fracture-induced weakening on coal mine gateroad stability, Int. J. Rock Mech. Min. 88 (2016) 307–317.

[7] N. Morita, A.D. Black, G.-F. Guh, Theory of lost circulation pressure, in: SPE Annual Technical Conference and Exhibition, Society of Petroleum Engineers, New Orleans, Louisiana, 1990.

[8] M.J. Economides, K.G. Nolte, Reservoir Stimulation, Vol. 2, Wiley, New York, 2000.

[9] B. Legarth, E. Huenges, G. Zimmermann, Hydraulic fracturing in a sedimentary geothermal reservoir: results and implications, Int. J. Rock Mech. Min. 42 (7–8) (2005) 1028–1041.

[10] A. Ghassemi, S. Tarasovs, A.H.-D. Cheng, A 3-D study of the effects of thermomechanical loads on fracture slip in enhanced geothermal reservoirs, Int. J. Rock Mech. Min. 44 (8) (2007) 1132–1148.

[11] K. Yoshioka, R.G. Pasikki, I. Suryata, K.L. Riedel, Hydraulic stimulation techniques applied to injection wells at the salak geothermal field, indonesia, in: SPE Western Regional Meeting, 2009.

[12] J. Adachi, E. Siebrits, J. Desroches, Computer simulation of hydraulic fractures, Int. J Rock Mech. Min. Sci. 44 (2007) 739–757.

[13] N.R. Warpinski, L.W. Teufel, Influence of geologic discontinuities on hydraulic fracture propagation, J. Petrol. Technol. 39 (02) (1987) 209–220.

[14] M.J. Mayerhofer, E. Lolon, N.R. Warpinski, C.L. Cipolla, D.W. Walser, C.M. Rightmire, What is stimulated reservoir volume? SPE Prod. Operat. 25 (01) (2010) 89–98.
[15] N. Watanabe, M. Egawa, K. Sakaguchi, T. Ishibashi, N. Tsuchiya, Hydraulic fracturing and permeability enhancement in granite from subcritical/brittle to supercritical/ductile conditions, Geo. Res. Lett. 44 (11) (2017) 5468–5475.
[16] Y. Yuan, Simulation of Penny-shaped Hydraulic Fracturing in Porous Media (PhD thesis), The University of Oklahoma, 1997.
[17] A. Ghassemi, Three-dimensional Poroelastic Hydraulic Fracture Simulation using Displacement Discontinuity Method (PhD thesis), The University of Oklahoma, 1996.
[18] T.J. Boone, A.R. Ingraffea, An investigation of poroelastic effects related to hydraulic fracture propagation in rock and stress measurement techniques, in: Proceeding os the 30th U.S. Symposium on Rock Mechanics (USRMS), ARMA-89-0073, 1989.
[19] B. Carrier, S. Granet, Numerical modeling of hydraulic fracture problem in permeable medium using cohesive zone model, Eng. Fracture Mech. 79 (2012) 312–328.
[20] J.M. Segura, I. Carol, On zero-thickness interface elements for diffusion problems, Int. J. Numer. Anal. Methods Geomech. 28 (9) (2004) 947–962.
[21] J.M. Segura, I. Carol, Coupled HM analysis using zero-thickness interface elements with double nodes. Part I: Theoretical model, Int. J. Numer. Anal. Methods Geomech. 32 (18) (2008) 2083–2101.
[22] J.M. Segura, I. Carol, Coupled HM analysis using zero-thickness interface elements with double nodes. Part II: Verification and application, Int. J. Numer. Anal. Methods Geomech. 32 (18) (2008) 2103–2123.
[23] T.J. Boone, A.R. Ingraffea, A numerical procedure for simulation of hydraulically driven fracture propagation in poroelastic media, Int. J. Numer. Anal. Methods. Geomech. 14 (1990) 27–47.
[24] M.C. Lobão, R. Eve, D.R.J. Owen, E.A. de Souza Neto, Modelling of hydro-fracture flow in porous media, Eng. Comput. 27 (1) (2010) 129–154.
[25] P. Gupta, C.A. Duarte, Simulation of non-planar three-dimensional hydraulic fracture propagation, Int. J. Numer. Anal. Methods Geomech. 38 (doi: 10.1002/nag.2305) (2014).
[26] M.M. Chiaramonte, E.S. Gawlik, H. Kabaria, A.J. Lew, Universal meshes for the simulation of brittle fracture and moving boundary problems, in: Innovative Numerical Approaches for Multi-Field and Multi-Scale Problems, Springer International Publishing, 2016, pp. 115–134.
[27] B. Lecampion, An extended finite element method for hydraulic fracture problems, Commun. Numer. Methods Eng. 25 (2009) 121–133.
[28] A. Dahi-Taleghani, J.E. Olson, Numerical modeling of multistranded-hydraulic-fracture propagation: accounting for the interaction between induced and natural fractures, SPE J. 16 (03) (2011) 575–581.
[29] E. Gordeliy, A. Peirce, Coupling schemes for modeling hydraulic fracture propagation using the xfem, Comput. Methods Appl. Mech. Engrg. 253 (2012) 1–53.
[30] K.H. Searles, M.G. Zielonka, J. Ning, J.L. Garzon, N.M. Kostov, P.F. Sanz, E. Biediger, Fully-coupled 3d hydraulic fracture models: development, validation, and application to o&G Problems, 2016.
[31] H. Ouchi, A. Katiyar, J. York, J.T. Foster, M.M. Sharma, A fully coupled porous flow and geomechanics model for fluid driven cracks: a peridynamics approach, Comput. Mech. 55 (3) (2015) 561–576.
[32] B. Damjanac, C. Detournay, P.A. Cundall, Application of particle and lattice codes to simulation of hydraulic fracturing, Comp. Part. Mech. 3 (2) (2016) 249–261.
[33] P. Xing, K. Yoshioka, J. Adachi, A. El-fayoumi, B. Damjanac, A.P. Bunger, Lattice simulation of laboratory hydraulic fracture containment in layered reservoirs, Comput. Geotech. 100 (November 2017) (2018) 62–75.
[34] G.A. Francfort, J.-J. Marigo, Revisiting brittle fracture as an energy minimization problem, J. Mech. Phys. Solids 46 (8) (1998) 1319–1342.
[35] B. Bourdin, G.A. Francfort, J.-J. Marigo, Numerical experiments in revisited brittle fracture, J. Mech. Phys. Solids 48 (4) (2000) 797–826.
[36] B. Bourdin, G.A. Francfort, J.-J. Marigo, The variational approach to fracture, J. Elasticity 91 (1–3) (2008) 5–148.
[37] B. Bourdin, C.J. Larsen, C.L. Richardson, A time-discrete model for dynamic fracture based on crack regularization, Int. J. Fracture 168 (2) (2011) 133–143.
[38] M.J. Borden, C.V. Verhoosel, M.A. Scott, T.J.R. Hughes, C.M. Landis, A phase-field description of dynamic brittle fracture, Comput. Methods Appl. Mech. Engrg. 217–220 (2012) 77–95.
[39] T. Li, J.-J. Marigo, D. Guilbaud, S. Potapov, Gradient damage modeling of brittle fracture in an explicit dynamic context, Internat. J. Numer. Methods Engrg. 00 (March) (2016) 1–25.
[40] M. Ambati, T. Gerasimov, L. De Lorenzis, Phase-field modeling of ductile fracture, Comput. Mech. 55 (5) (2015) 1017–1040.
[41] C. Miehe, S. Mauthe, S. Teichtmeister, Minimization principles for the coupled problem of darcy-biot-type fluid transport in porous media linked to phase field modeling of fracture, in: Journal of the Mechanics and Physics of Solids, J. Mech. Phys. Solids 82 (2015) 186–217.
[42] R. Alessi, J.-J. Marigo, C. Maurini, S. Vidoli, Coupling damage and plasticity for a phase-field regularisation of brittle, cohesive and ductile fracture: one-dimensional examples, Int. J. Mech. Sci. (2017) 1–18.
[43] C. Maurini, B. Bourdin, G. Gauthier, V. Lazarus, Crack patterns obtained by unidirectional drying of a colloidal suspension in a capillary tube: experiments and numerical simulations using a two-dimensional variational approach, Int. J. Fracture 184 (1–2) (2013) 75–91.
[44] B. Bourdin, J.-J. Marigo, C. Maurini, P. Sicsic, Morphogenesis and propagation of complex cracks induced by thermal shocks, Phys. Rev. Lett. 112 (1) (2014) 1–5.
[45] C. Miehe, S. Mauthe, Phase field modeling of fracture in multi-physics problems. part iii. crack driving forces in hydro-poro-elasticity and hydraulic fracturing of fluid-saturated porous media, Comput. Methods Appl. Mech. Engrg. 304 (2016) 619–655.
[46] B. Bourdin, C. Chukwudozie, K. Yoshioka, A variational approach to the numerical simulation of hydraulic fracturing, in: SPE ATCE 2012, 2012.
[47] C. Chukwudozie, B. Bourdin, K. Yoshioka, A variational approach to the modeling and numerical simulation of hydraulic fracturing under in-situ stresses, in: Proceedings of the 38th Workshop on Geothermal Reservoir Engineering, 2013.

[48] M.F. Wheeler, T. Wick, W. Wollner, An augmented-lagrangian method for the phase-field approach for pressurized fractures, Comput. Methods Appl. Mech. Engrg. 271 (2014) 69–85.
[49] A. Mikelić, M.F. Wheeler, T. Wick, A quasi-static phase-field approach to pressurized fractures, Nonlinearity 28 (5) (2015) 1371–1399.
[50] T. Heister, M.F. Wheeler, T. Wick, A primal-dual active set method and predictor-corrector mesh adaptivity for computing fracture propagation using a phase-field approach, Comput. Methods Appl. Mech. Engrg. 290 (2015) 466–495.
[51] A. Mikelić, M.F. Wheeler, T. Wick, A phase-field method for propagating fluid-filled fractures coupled to a surrounding porous medium, Multiscale Model. Simul. 48 (1) (2015) 162–186.
[52] A. Mikelić, M.F. Wheeler, T. Wick, Phase-field modeling of a fluid-driven fracture in a poroelastic medium, Computat. Geosci. 19 (6) (2015) 1171–1195.
[53] D. Santillán, R. Juanes, L. Cueto-Felgueroso, Phase field model of fluid-driven fracture in elastic media: immersed-fracture formulation and validation with analytical solutions, J. Geophus. Res.-Sol Ea. (2017).
[54] L. Xia, J. Yvonnet, S. Ghabezloo, Phase field modeling of hydraulic fracturing with interfacial damage in highly heterogeneous fluid-saturated porous media, Eng. Fract. Mech. 186 (October) (2017) 158–180.
[55] S. Lee, M.F. Wheeler, T. Wick, Iterative coupling of flow, geomechanics and adaptive phase-field fracture including level-set crack width approaches, J. Comput. Appl. Math. 314 (2017) 40–60.
[56] Z.A. Wilson, C.M. Landis, Phase-field modeling of hydraulic fracture, J. Mech. Phys. Solids 96 (2016) 264–290.
[57] W. Ehlers, C. Luo, A phase-field approach embedded in the theory of porous media for the description of dynamic hydraulic fracturing, Comput. Methods Appl. Mech. Engrg. 315 (2017) 348–368.
[58] Y. Heider, B. Markert, A phase-field modeling approach of hydraulic fracture in saturated porous media, Mech. Res. Commun. 80 (2017) 38–46.
[59] T. Wick, G. Singh, M.F. Wheeler, Fluid-filled fracture propagation with a phase-field approach and coupling to a reservoir simulator, SPE J. 21 (03) (2016) 0981–0999.
[60] K. Yoshioka, B. Bourdin, A variational hydraulic fracturing model coupled to a reservoir simulator, Int. J. Rock Mech. Min. 88 (2016) 137–150.
[61] E. Detournay, D.I. Garagash, The near tip region of a fluid driven fracture propagating in a permeable elastic solid, J. Fluid Mech. 494 (2003) 1–32.
[62] C. Serres, C. Alboin, J. Jaffre, J. Roberts, Modeling Fractures as Interfaces for Flow and Transport in Porous Media, Technical report, Inst. de Radioprotection et de Surete Nucleaire, Dept. d'Evaluation de Surete, 92-Fontenay aux Roses (France), 2002.
[63] V. Martin, J. Jaffré, J.E. Roberts, Modeling fractures and barriers as interfaces for flow in porous media, SIAM J. Sci. Comput. 26 (5) (2005) 1667–1691.
[64] G.K. Batchelor, An Introduction to Fluid Dynamics, Cambridge University Press, 1967.
[65] M.A. Biot, General theory of three-dimensional consolidation, J. Appl. Phys. 12 (2) (1941) 155–164.
[66] R.W. Lewis, The Finite Element Method in Static and Dynamic Deformation and Consolidation of Porous Media, John Wiley and Sons, Ltd, 1998.
[67] Y. Zheng, R. Burridge, D.R. Burns, Reservoir simulation with the finite element method using Biot poroelastic approach, in: Technical report, Massachusetts Institute of Technology. Earth Resources Laboratory, 2003.
[68] A. Settari, A new general model of fluid loss in hydraulic fracturing, SPE J. 25 (04) (1985) 491–501.
[69] E.D. Carter, in: American Petroleum Institute (Ed.), Drilling and Production Practices, G.C. Howard, C.R. Fast, Tulsa, OK, 1957 pp. 261–270.
[70] John Carl Gottschling, Marcellus net fracturing pressure analysis, in: SPE Eastern Regional Meeting, Society of Petroleum Engineers, Morgantown, West Virginia, USA, 2010.
[71] L. Ambrosio, V.M. Tortorelli, Approximation of functional depending on jumps by elliptic functional via Γ–convergence, Comm. Pure Appl. Math. 43 (8) (1990) 999–1036.
[72] L. Ambrosio, V.M. Tortorelli, On the approximation of free discontinuity problems, Boll. Un. Mat. Ital. B (7) 6 (1) (1992) 105–123.
[73] A. Braides, Approximation of free-discontinuity problems, Lecture Notes in Mathematics, vol. 1694, Springer, 1998.
[74] L.C. Evans, R.F. Gariepy, Measure Theory and Fine Properties of Functions, CRC Press, Boca Raton, FL, 1992, p. viii+268.
[75] K. Pham, H. Amor, J.-J. Marigo, C. Maurini, Gradient damage models and their use to approximate brittle fracture, Int. J. Damage Mech. 20 (4, SI) (2011) 618–652.
[76] J.-J. Marigo, C. Maurini, K. Pham, An overview of the modelling of fracture by gradient damage models, Meccanica 51 (12) (2016) 3107–3128.
[77] E. Tanné, T. Li, B. Bourdin, J-J. Marigo, C. Maurini, Crack nucleation in variational phase-field models of brittle fracture, J. Mech. Phys. Solids 110 (2018) 80–99.
[78] S. Balay, S. Abhyankar, M.F. Adams, J. Brown, P. Brune, K. Buschelman, L Dalcin, V. Eijkhout, W.D. Gropp, D. Kaushik, M.G. Knepley, D.A. May, L.C. McInnes, K. Rupp, B.F. Smith, S. Zampini, H. Zhang, H. Zhang, Petsc Web page, 2017.
[79] S. Balay, S. Abhyankar, M.F. Adams, J. Brown, P. Brune, K. Buschelman, L. Dalcin, V. Eijkhout, W.D. Gropp, D. Kaushik, M.G. Knepley, D.A. May, L.C. McInnes, K. Rupp, P. Sanan, B.F. Smith, S. Zampini, H. Zhang, H. Zhang, PETSc Users Manual, Technical Report ANL-95/11 - Revision 3.8, Argonne National Laboratory, 2017.
[80] A. Mikelić, M.F. Wheeler, Convergence of iterative coupling for coupled flow and geomechanics, Computat. Geosci. 17 (3) (2013) 455–461.
[81] J. Kim, H.A. Tchelepi, R. Juanes, Stability and convergence of sequential methods for coupled flow and geomechanics: drained and undrained splits, Comput. Methods Appl. Mech. Engrg. 200 (2011) 2094–2216.
[82] I.N. Sneddon, M. Lowengrub, Crack Problems in the Classical Theory of Elasticity, John Wiley & Sons, 1969.
[83] J. Hu, D.I. Garagash, Plane-strain propagation of a fluid-driven crack in a permeable rock with fracture toughness, J. Eng. Mech. (2010).

[84] D.I. Garagash, Plane-strain propagation of a fluid-driven fracture during injection and shut-in: asymptotics of large toughness, Eng. Fract. Mech. 73 (4) (2006) 456–481.
[85] E. Tanné, Variational Phase-field Models from Brittle to Ductile Fracture: Nucleation and Propagation PhD thesis, Université Paris-Saclay, École Polytechnique, 2017.
[86] E. Tanné, C. Chukwudozie, B. Bourdin, K. Yoshioka, Loss of symmetry in network of hydraulic cracks in the toughness-dominated regime, In preparation, 2019.